Atmos. Meas. Tech., 9, 4103–4122, 2016
www.atmos-meas-tech.net/9/4103/2016/
doi:10.5194/amt-9-4103-2016

Atmospheric Measurement Techniques
Open Access
EGU

Limb–nadir matching using non-coincident NO_2 observations: proof of concept and the OMI-minus-OSIRIS prototype product

Cristen Adams[1,2], Elise N. Normand[1], Chris A. McLinden[3], Adam E. Bourassa[1], Nicholas D. Lloyd[1], Douglas A. Degenstein[1], Nickolay A. Krotkov[4], Maria Belmonte Rivas[5], K. Folkert Boersma[5,6], and Henk Eskes[5]

[1]Institute of Space and Atmospheric Studies, University of Saskatchewan, Saskatoon, Canada
[2]Alberta Environmental Monitoring and Science Division, Alberta Environment and Parks, Edmonton, Canada
[3]Air Quality Research Division, Environment Canada, Toronto, Ontario, Canada
[4]NASA Goddard Space Flight Center, Greenbelt, MD, USA
[5]Royal Netherlands Meteorological Institute (KNMI), De Bilt, the Netherlands
[6]Wageningen University, Meteorology and Air Quality Group, Wageningen, the Netherlands

Correspondence to: Cristen Adams (cristenlfadams@gmail.com)

Received: 21 April 2016 – Published in Atmos. Meas. Tech. Discuss.: 4 May 2016
Revised: 4 August 2016 – Accepted: 8 August 2016 – Published: 26 August 2016

Abstract. A variant of the limb–nadir matching technique for deriving tropospheric NO_2 columns is presented in which the stratospheric component of the NO_2 slant column density (SCD) measured by the Ozone Monitoring Instrument (OMI) is removed using non-coincident profiles from the Optical Spectrograph and InfraRed Imaging System (OSIRIS). In order to correct their mismatch in local time and the diurnal variation of stratospheric NO_2, OSIRIS profiles, which were measured just after sunrise, were mapped to the local time of OMI observations using a photochemical box model. Following the profile time adjustment, OSIRIS NO_2 stratospheric vertical column densities (VCDs) were calculated. For profiles that did not reach down to the tropopause, VCDs were adjusted using the photochemical model. Using air mass factors from the OMI Standard Product (SP), a new tropospheric NO_2 VCD product – referred to as OMI-minus-OSIRIS (OmO) – was generated through limb–nadir matching. To accomplish this, the OMI total SCDs were scaled using correction factors derived from the next-generation SCDs that improve upon the spectral fitting used for the current operational products. One year, 2008, of OmO was generated for 60° S to 60° N and a cursory evaluation was performed. The OmO product was found to capture the main features of tropospheric NO_2, including a background value of about 0.3×10^{15} molecules cm^{-2} over the tropical Pacific and values comparable to the OMI operational products over anthropogenic source areas. While additional study is required, these results suggest that a limb–nadir matching approach is feasible for the removal of stratospheric NO_2 measured by a polar orbiter from a nadir-viewing instrument in a geostationary orbit such as Tropospheric Emissions: Monitoring of Pollution (TEMPO) or Sentinel-4.

1 Introduction

Nadir satellite instruments can measure daily global maps of tropospheric nitrogen dioxide (NO_2), which, at the surface, is a pollutant linked to smog and acid rain. Tropospheric NO_2 was first successfully retrieved from the Global Ozone Monitoring Experiment (GOME) (Burrows et al., 1999) and has since also been measured by the Scanning Imaging Absorption Spectrometer for Atmospheric Chartography (SCIAMACHY) (Bovensmann et al., 1999), Ozone Monitoring Instrument (OMI) (Levelt et al., 2006), and GOME 2 (Callies et al., 2000) nadir-viewing instruments. The next generation of nadir instruments will be on geostationary platforms such as the Tropospheric Emissions: Monitoring of Pollution (TEMPO) (Zoogman et al., 2016), Sentinel-4 (Ingmann et al., 2012), and Geostationary Environmental Monitoring Spectrometer (Kim, 2012). These instruments will measure air pollution at much higher spatial and temporal resolution, allowing for the study of the diurnal cycle of emissions and chemistry at a suburban scale.

High concentrations of NO_2 are found in the stratosphere, where NO_2 has a large seasonal and diurnal variability due to photochemistry and, in some case, due to dynamics as well (e.g., Dirksen et al., 2011). Therefore retrievals for tropospheric NO_2 from nadir instruments typically rely on extrapolation or assimilation approaches to determine the stratospheric contribution to NO_2. A correct and unbiased removal of stratospheric NO_2 is a major challenge and represents a significant source of uncertainty in tropospheric NO_2 retrieval products. In this proof-of-concept study, we investigate the possibility of deriving tropospheric NO_2 by matching non-coincident measurements from limb-viewing satellite instruments with nadir-viewing instruments. Similar techniques could be applied to future geostationary missions, which will take measurements across a range of local times.

Various methods have been used to separate stratospheric and tropospheric contributions from the total NO_2 vertical column density (VCD) measured by nadir satellites. Several of these techniques assume that the NO_2 distribution over a remote, non-polluted location, like the Pacific Ocean, is dominated by the stratospheric component. These stratospheric NO_2 values are then extrapolated to other locations. Hilboll et al. (2013) give a good overview of the development of these methods from early analyses, which assumed that stratospheric NO_2 does not vary within a latitude band (Martin et al., 2002; Richter and Burrows, 2002) to more complex techniques, such as the planetary wave-2 zonal analysis technique (Bucsela et al., 2006). Chemical transport model information can also be used to infer stratospheric NO_2. In order to account for biases between the modelled stratosphere and the satellite measurements, the model data can be scaled to the satellite measurements through comparisons in the Pacific Ocean (Richter et al., 2005) or the measured total column NO_2 can be assimilated in the model (e.g., Boersma et al., 2007). These techniques, as applied to operational data products for OMI, are described in more detail in Sect. 2.1. Another approach is the cloud slicing method (Belmonte Rivas et al., 2015; Choi et al., 2014), which yields information on the NO_2 vertical profile. When there is cloud cover, the lower part of the atmosphere is obscured, so the levels of NO_2 in various layers of the atmosphere above the clouds can be inferred. This approach is not currently used for any operational data products.

Another promising technique involves using the global, vertically resolved stratospheric NO_2 profiles from satellite instruments that measure in the limb-viewing geometry. Near-daily global resolution can be obtained using limb instruments that measure scattered sunlight, such as the Optical Spectrograph and InfraRed Imaging System (OSIRIS) (Llewellyn et al., 2004; McLinden et al., 2012b) and SCIAMACHY (Bovensmann et al., 1999), as well as instruments that measure emissions, such as the Michelson Interferometer for Passive Atmospheric Sounding (MIPAS) (Fischer et al., 2008) and the High Resolution Dynamics Limb Sounder (HIRDLS) (Gille et al., 2008). These limb-viewing measurements of stratospheric NO_2 can then be matched to and subtracted from the nadir total column measurement.

The limb–nadir matching method has been employed for SCIAMACHY NO_2 (Beirle et al., 2010; Hilboll et al., 2013; Sierk et al., 2006; Sioris et al., 2004), which provides both limb and nadir measurements from the same instrument virtually simultaneously and at the same local time. In the most recent analysis, Hilboll et al. (2013) calculate a stratospheric NO_2 VCD from limb measurements for each nadir measurement. They adjust the stratospheric VCDs to match the levels observed in the nadir columns using a latitude-dependent factor calculated daily over the Pacific Ocean, where levels of tropospheric NO_2 are expected to be low. Since the SCIAMACHY limb- and nadir-viewing geometries measure at the same local time, the diurnal variation of NO_2 does not complicate the limb–nadir matching.

In this proof-of-concept study, the potential of deriving tropospheric NO_2 from measurements taken by limb and nadir instruments at different local times is explored. OSIRIS limb-viewing stratospheric NO_2 from the descending node of the orbit, measured toward sunrise, and OMI nadir-viewing column NO_2, measured near midday, are used to quantify the abundance of tropospheric NO_2. OMI tropospheric NO_2 has been well characterized against other instruments (Boersma et al., 2011; Lamsal et al., 2014) and has been used in many scientific studies of tropospheric air pollution (e.g., Duncan et al., 2016; Krotkov et al., 2016; McLinden et al., 2012a; Russell et al., 2012; Veefkind et al., 2011; Zhou et al., 2012) as well as some work on stratospheric NO_2 (e.g., Dirksen et al., 2011). OSIRIS stratospheric NO_2 agrees well with other instruments (Brohede et al., 2007; Kerzenmacher et al., 2008) and provides daily near-global coverage, which is necessary to match to OMI measurement dates and locations. The resulting tropospheric VCDs are referred to as the OMI-minus-OSIRIS (OmO) data product.

Although the local time mismatch between OSIRIS and OMI adds a significant complication due to the diurnal nature of NO_2, it is also a more realistic scenario in the merging of limb measurements for future geostationary missions, which will measure throughout the day across a range of local times. Ideally, a limb–nadir merging would be carried out through a data assimilation system, but it is important nonetheless to understand their compatibility in a much simpler framework.

In order to create the OmO dataset, the following steps were taken. OSIRIS, OMI, and photochemical model data were used, as described in Sect. 2. A series of 3-day average stratospheric VCD maps on a uniform latitude and longitude grid were created from OSIRIS data for various local times, using scale factors from the photochemical model, as described in Sect. 3. The OmO data product was then calculated using OMI VCDs and air mass factors (AMFs), along with matched stratospheric VCDs interpolated from the OSIRIS VCD maps. These calculations and a correction factor for a known bias in the OMI data (Marchenko et al., 2015; van

Geffen et al., 2015), as well as an assessment of the OmO prototype data, are described in Sect. 4. A discussion of these results and future applications is given Sect. 5.

2 Measurements and modelling tools

2.1 OMI on Aura

OMI (Levelt et al., 2006) is a nadir-viewing solar backscatter spectrometer on board the Aura satellite (Schoeberl et al., 2006), which was launched into a polar orbit about the Earth on 15 July 2004. The satellite was designed to further our understanding of stratospheric and tropospheric chemistry as well as climate systems through high spectral resolution measurements in the UV/visible (270–500 nm). OMI follows a sun-synchronous orbit with a 98.2° inclination and an ascending equatorial node crossing of approximately 13:45 local time (LT). OMI captures a 114° field of view, which covers a width of 2600 km. The swath direction is perpendicular to the satellite flight path, so with 14 orbits per day there is near complete global coverage. There are a total of 60 binned pixel positions across the entire swath with an outermost swath angle of 57°. In the centred nadir position, the ground pixel size covers $13 \times 24\,km^2$ (along track by across track) for the UV-2 and visible channels and $13 \times 48\,km^2$ for the UV-1 channel. As the swath angle increases, the pixel footprint increases to a maximum of $\sim 15 \times 150\,km^2$ at the outermost pixel positions. NO_2 is retrieved with the visible channel between 405 and 465 nm, where there is little interference from other absorbers.

There are two operational NO_2 data products: the Dutch OMI NO_2 (DOMINO v2) product (Boersma et al., 2011) and the NASA standard product (SP v2) (Bucsela et al., 2013). These two data products are referred to as OMI-SP and OMI-DOMINO, respectively, throughout this paper. Both products employ a multi-step approach with a common first step. Differential optical absorption spectroscopy (DOAS) is used to determine the NO_2 slant column densities (SCDs) by fitting the ratio of earthshine radiance to extraterrestrial irradiance spectra to the laboratory reference data, Ring spectrum (Chance and Spurr, 1997), and polynomial. Physically, the SCD represents the total absorption by NO_2 along the average path of the sunlight through the atmosphere, which includes absorption in both the stratosphere and troposphere.

Different approaches are used for the second step, which is to execute the stratosphere–troposphere separation. OMI-DOMINO accomplishes stratosphere–troposphere separation by assimilating the OMI slant columns within the TM4 chemistry-transport model (Boersma et al., 2007; Dirksen et al., 2011), effectively determining how much NO_2 resides in the stratosphere, which is then subtracted from the total slant column. For OMI-SP, the stratospheric column is recovered by performing a local analysis of the stratospheric field in cloudy regions or regions where there is no tropospheric pollution. These values are then extrapolated to polluted regions using a spatial interpolation and smoothing technique (Bucsela et al., 2013), which assumes that changes in tropospheric NO_2 occur on relatively shorter geographical scales than stratospheric ones.

The final step for both operational NO_2 data products is the determination of the tropospheric VCD from the residual SCD in the troposphere. In general, the total SCD, S, is related to the total VCD, V, through the tropospheric AMF, A, by $S = V \times A$ and is a measure of the changes in absorption when light traverses an effective or "slant" path through a tropospheric layer. The AMF is dependent on the path length, which in turn depends on the solar zenith angle (SZA), solar azimuth angle, the satellite viewing angle, the vertical distribution of absorbing species, cloud and aerosol properties, and albedo. In the troposphere, a key dependence is the vertical distribution of NO_2 which is taken from model simulations: the TM4 model (at the time of the measurement) for the DOMINO product and the Global Modeling Initiative (GMI) model (monthly) for the SP product. AMFs are calculated using radiative transfer models that accurately simulate absorption, multiple scattering, and reflection off the surface.

The OmO prototype dataset was constructed using the AMFs and VCDs from the OMI-SP v2 data files (Bucsela et al., 2013), using the methodology given in Sect. 4.3. An alternate OmO-DOMINO prototype was also constructed using OMI-DOMINO v2.0 (Boersma et al., 2011) AMFs and VCDs. The OSIRIS stratospheric VCDs and OmO tropospheric VCDs were compared with both OMI-SP and OMI-DOMINO v2.0. For all figures and statistics presented in this paper, OMI and OmO data for OMI cloud radiance fractions < 0.3 and SZA $< 75°$ were used. Additionally, OMI pixels affected by the row anomaly were removed. Note that both the OMI-SP and OMI-DOMINO retrieval algorithms correct for across-track variability, or stripes, for pixels that are not affected by the row anomaly.

2.2 OSIRIS on Odin

OSIRIS (Llewellyn et al., 2004; McLinden et al., 2012b) measures the atmospheric limb radiance of scattered sunlight as a function of tangent altitude from the upper troposphere to the lower mesosphere. This Canadian instrument is on board Odin (Murtagh et al., 2002), a Swedish satellite, which was launched 20 February 2001 into a sun-synchronous orbit near 600 km in altitude with about a 90 min period. The satellite track is near terminator and closely follows the local dusk and dawn terminators on the ascending and descending tracks with northward and southward equatorial crossings at 18:00 and 06:00 LT, respectively. OSIRIS has near-global coverage from 82° S to 82° N with an orbital inclination of 98° from the Equator. At the tangent point, the atmosphere is in darkness when the SZA is greater than 90°; the winter hemisphere is largely darkened at the local time of the measurements.

OSIRIS includes an optical spectrograph, which comprises an optical grating and a charge-coupled device detector, and an infrared imager. Atmospheric limb radiance is measured by the optical spectrograph between 280 and 810 nm with a spectral resolution of about 1 nm. Vertical profiles from approximately 7 to 110 km in tangent altitude are acquired by nodding the spacecraft. The field of view at the tangent point is roughly $40 \times 1\,km^2$ (horizontal by vertical) and successive measurements are separated by about 2 km tangent altitude.

In this work, stratospheric profiles from the v5.0 NO_2 dataset (Haley and Brohede, 2007) were used. Slant column densities are retrieved in the 435–451 nm range, using the DOAS technique. NO_2 profiles are then retrieved using an optimal estimation technique on a fixed retrieval grid, from 10 to 46 km at 2 km intervals. The OSIRIS NO_2 stratospheric VCDs agree to within 0.25×10^{15} molecules cm^{-2} of the other limb instruments for most latitudes and seasons, as shown in Appendix A.

OSIRIS data from the descending node only were used in this analysis. Due to the diurnal variation of NO_2, there are systematic differences between descending and ascending track measurements, which are taken at morning and evening local times, respectively. The descending node was selected because in the ascending node OSIRIS measures at larger SZAs, leading to fewer valid measurements in the winter hemisphere. Furthermore, the solar scattering angle on the ascending track is closer to the forward scattering scenario, which causes clouds and aerosols to appear very bright, leading to the saturation of pixels and the rejection of some measurements.

Additionally, only data for $SZA < 88°$ were used. This largely eliminates errors introduced by the "diurnal effect", also called "chemical enhancement" (Hendrick et al., 2006; McLinden et al., 2006), which is not currently accounted for in the NO_2 retrieval. This occurs because sunlight passes through a range of SZAs in the atmosphere before reaching the OSIRIS instrument and therefore samples NO_2 at different points in its diurnal cycle. This effect is largest toward $SZA = 90°$, where NO_2 varies rapidly.

The 2008 period was chosen because it covers the time when the descending node measurement time drifts closest to 07:00 before the sampling time drifts back toward 06:00. This maximises the number of valid descending node measurements.

2.3 Photochemical box model

In this work, a stratospheric photochemical box model (Brohede et al., 2008; McLinden et al., 2000; Prather, 1992) is employed to simulate the NO_2 diurnal cycle (see Sect. 3.1) and to adjust OSIRIS stratospheric VCDs for NO_2 profiles that terminate above the tropopause (see Sect. 3.2). For a particular simulation, the background pressure and temperature atmospheric profiles, ozone, long-lived tracers (N_2O, H_2O, CH_4), and the NO_y, Cl_y, and Br_y families need to be specified for each altitude of the OSIRIS profiles. All remaining species are calculated to be in a 24 h steady state by integrating the model over 30 days, but fixed to a given Julian day. Heterogeneous chemistry on background stratospheric aerosols is prescribed by the model, but no polar stratospheric clouds are included.

For the present study, the photochemical model was run at each altitude layer of every OSIRIS NO_2 profile measurement. N_2O, CH_4, NO_y, Cl_y, and Br_y from the Canadian Middle Atmosphere Model (CMAM) (Jonsson et al., 2004; Scinocca et al., 2008) were interpolated to the month and latitude of the OSIRIS NO_2 measurement. H_2O was derived from tracer correlations with CH_4 (McLinden et al., 2000). OSIRIS ozone profiles (Degenstein et al., 2009), measured at the same time as NO_2, were included in the analysis. Outside of the OSIRIS ozone altitude range and for scans with missing ozone data, the CMAM ozone climatology (Jonsson et al., 2004; Scinocca et al., 2008) was used. Albedo was also from OSIRIS retrievals (Degenstein et al., 2009) from the same scan as the NO_2 measurement. Aerosol extinction was interpolated from 2-week OSIRIS aerosol extinction averages (Rieger et al., 2015) and converted to aerosol surface area assuming a lognormal distribution with a mode radius of 80 nm and a mode width of 1.6, which is consistent with the OSIRIS aerosol retrieval assumptions. Pressure and temperature profiles were obtained from the European Centre for Medium-Range Weather Forecasts (ECWMF) analysis data for the time and location of each OSIRIS scan.

Validation of individual profiles from the box model, constrained in an analogous manner, was performed using MkIV balloon measurements (Brohede et al., 2008). Additional, albeit indirect, verification of the model's ability to adjust from one LST to another can be seen in the numerous satellite NO_2 validation studies for which this approach has been used, including the original OSIRIS NO_2 work (Brohede et al., 2007), Atmospheric Chemistry Experiment Fourier transform spectrometer (ACE-FTS) NO_2 (Kerzenmacher et al., 2008), as well as what is provided in Appendix A.

3 OSIRIS stratospheric VCD maps

In order to create the OmO data product, stratospheric VCDs must be available at the latitude, longitude, date, and local time of each OMI measurement. Therefore, individual OSIRIS stratospheric profiles were extrapolated to a uniform grid of local times using the photochemical box model and stratospheric VCDs were calculated from these profiles. The stratospheric VCDs were gridded uniformly in space and time, so that they could be interpolated to OMI measurements latitude, longitude, date, and local time. The detailed procedure used to create the OSIRIS stratospheric VCD maps is described in this section.

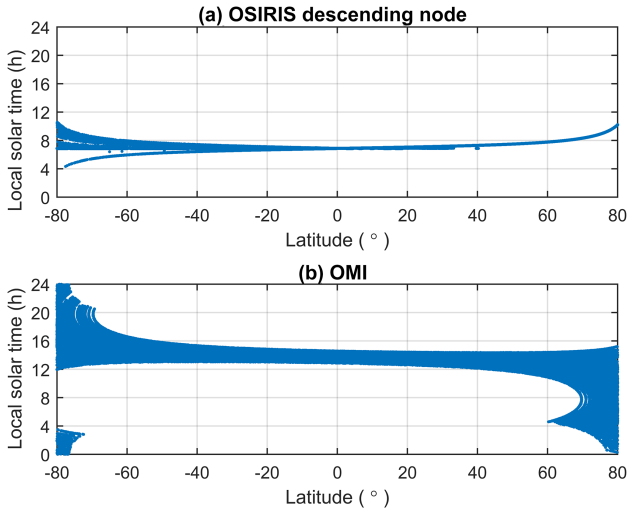

Figure 1. Local solar time versus latitude for **(a)** OSIRIS descending node and **(b)** OMI measurements in 2008. OSIRIS local times are for all profiles in 2008. OMI local times are sampled for 1 day in each month.

3.1 Scaling the local time of OSIRIS measurements

A key challenge in comparing and merging measurements of stratospheric NO_2 made at different local times lies in reconciling the impact of its diurnal cycle due to photochemistry. For a detailed description of the diurnal variation of NO_2 and its impact on comparisons between satellite instruments, see, e.g., Belmonte Rivas et al. (2014). Over short timescales ($\sim$ 1 min), NO_2 and NO are in fast photochemical equilibrium and are referred to as NO_x. Since NO is produced by the photolysis of NO_2, more NO_x is in the form of NO_2 when there is less available sunlight. Therefore, levels of NO_2 are typically lower during the day than overnight, with sharp gradients over sunrise and sunset. Furthermore, slower reactions affect the overall amount of NO_x available. The most significant of these reactions is the reaction with N_2O_5, which occurs over longer timescales ($\sim$ hours to days): overnight NO_x is converted to N_2O_5 and during the day it is released again, causing the amount of NO_2 at sunset to be higher than the amount of NO_2 at sunrise.

The local times of OSIRIS and OMI measurements are shown in Fig. 1. At most latitudes, OSIRIS measurements are taken at local times in the morning, while OMI measurements are taken in the early afternoon. This affects the matching of OSIRIS and OMI datasets for the calculation of the OmO data product. For example, at low latitudes, OSIRIS descending node measurements are taken shortly after sunrise when, due to the photochemistry described above, there is less NO_2 in the stratosphere than during the OMI afternoon measurements. Therefore, the diurnal variation of NO_2 must be accounted for before subtracting OSIRIS stratospheric NO_2 from the OMI measurements.

The photochemical box model (see Sect. 2.3) was used to adjust, or map, the local time by applying a photochemical scaling factor to each layer in the profile (z). This is shown in Eq. (1):

$$\rho_{\mathrm{OSIRIS}}(z, t_{\mathrm{new}}, \mathrm{lat}, \mathrm{doy}) = \rho_{\mathrm{OSIRIS}}(z, t_{\mathrm{OSIRIS}}, \mathrm{lat}, \mathrm{doy}) \cdot \frac{\rho_{\mathrm{model}}(z, t_{\mathrm{new}}, \mathrm{lat}, \mathrm{doy})}{\rho_{\mathrm{model}}(z, t_{\mathrm{OSIRIS}}, \mathrm{lat}, \mathrm{doy})}, \quad (1)$$

where ρ_{OSIRIS} and ρ_{model} are the OSIRIS and modelled NO_2 number densities at a given altitude layer, respectively; t_{OSIRIS} and t_{new} are the local times of the OSIRIS measurement and the new adjusted time; lat is the latitude; and doy is the day of year. The box model time steps are calculated from the sine of the SZA, for a total of 49 time steps per day. Therefore, toward twilight, when NO_2 varies rapidly, there is better temporal resolution than toward noon. The t_{new} grid is at an hourly resolution, as discussed in Sect. 3.3.

This approach has been successfully applied using the same photochemical box model to the validation of NO_2 profiles (Brohede et al., 2007) and the merging of data products (Brohede et al., 2008). One advantage to this approach is that the photochemical box model provides high temporal resolution at twilight, when NO_2 is changing rapidly. Chemical transport models often have coarse spatial resolution (e.g., 1–3°), which can lead to errors in photochemical representation close to the terminator. Additionally, chemical transport models often have time steps of $\sim$ 10 min. For this study, these errors are unlikely to be a major factor as OSIRIS measurements are for SZA $< 88°$ and OMI measurements are for SZA $< 75°$. Another advantage is that we are able to, on a profile-by-profile basis, constrain the diurnal cycle with accurate and simultaneously measured ozone profiles as well as measurement-based representations of other input parameters.

3.2 OSIRIS stratospheric VCD calculations

Stratospheric NO_2 VCDs were calculated from OSIRIS profiles that had been adjusted to the desired local time. When NO_2 profile data are available from the tropopause (z_{trop}) to the top of the atmosphere (z_{toa}), the stratospheric VCD is the integral of the NO_2 number densities over altitude layers, as shown in Eq. (2).

$$V_{\mathrm{strat}} = \int_{z_{\mathrm{trop}}}^{z_{\mathrm{toa}}} \rho(z)\,\mathrm{d}z \quad (2)$$

OSIRIS v5.0 NO_2 profiles extend to 46 km, which is effectively the top of atmosphere in this context since NO_2 number densities are very low above this altitude. The altitude of the thermal tropopause was calculated using lapse rates from the National Center for Environmental Prediction (NCEP) reanalysis data (Kalnay et al., 1996). The OMI-DOMINO algorithm also uses the thermal tropopause (Dirksen et al., 2011),

but the OMI-SP algorithm uses a dynamical tropopause definition (Bucsela et al., 2013). The method used to calculate the tropopause is expected to have a minimal impact on stratospheric VCDs because concentrations of NO_2 are small near the tropopause. Furthermore, the tropopause definition was found to have very little effect on the OMI-SP retrievals (Bucsela et al., 2013).

For OSIRIS profiles that extend to or below the thermal tropopause, the NO_2 number density was interpolated to the tropopause altitude and a trapezoidal integration was performed from the tropopause to the top of the NO_2 profile to calculate the stratospheric VCD. Some OSIRIS profiles terminate above the tropopause and, therefore, information from the photochemical model was used to calculate the full stratospheric VCD, as shown in Eq. (3):

$$V_{\text{strat}} = V_{\text{part}}^{\text{OSIRIS}} \cdot \left(\frac{V_{\text{strat}}^{\text{model}}}{V_{\text{part}}^{\text{model}}} \right). \quad (3)$$

The modelled stratospheric VCD $\left(V_{\text{strat}}^{\text{model}}\right)$ was integrated using the same technique as for the OSIRIS profiles that extend below the tropopause (Eq. 2). Partial VCDs from the OSIRIS $\left(V_{\text{part}}^{\text{OSIRIS}}\right)$ and model profiles $\left(V_{\text{part}}^{\text{model}}\right)$ were calculated by a summation over the altitude layers with available OSIRIS NO_2 measurements, as shown in Eq. (4):

$$V_{\text{part}} = \sum_{z_{\min}}^{z_{\max}} \rho\left(z_i\right) \cdot \Delta z, \quad (4)$$

where $z_{\min}$ and $z_{\max}$ are the minimum and maximum altitude levels of available NO_2 data in the given OSIRIS profile and Δz is the altitude difference between OSIRIS profile layers, which is 2 km for the OSIRIS v5.0 NO_2 dataset. This summation technique was chosen for the calculation of the partial stratospheric columns because, compared with a trapezoidal integration, this maximised the amount of information coming from the lowermost available layer of the OSIRIS measurements.

Figure 2 shows statistics for the lowest altitude of the OSIRIS measurement relative to the thermal tropopause for individual scans. Negative altitude differences indicate that OSIRIS measured to altitudes below the thermal tropopause. Positive altitude differences indicate that the OSIRIS profiles terminated above the thermal tropopause and that therefore the OSIRIS VCDs were scaled to the full atmosphere using Eq. (3). For 45° S to 45° N, median altitude differences are negative, indicating the more than 50 % of the profiles reach the tropopause. Between 65° S and 55° N, 75 % of the profiles reach within 4 km of the tropopause. At high latitudes, the tropopause can be very low and therefore more OSIRIS profiles terminate higher above the tropopause. In order to avoid relying too heavily on the model scale factors at high latitudes, the OmO data product was calculated between 60° S and 60° N only. Additionally, profiles that terminate > 5 km above the tropopause were excluded from the analysis.

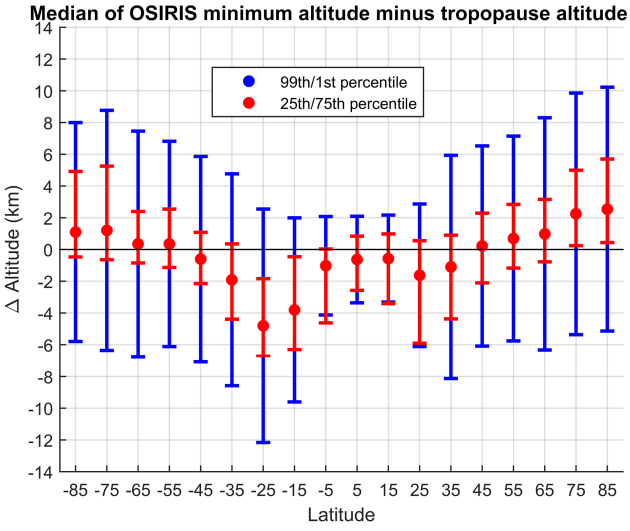

Figure 2. Difference between OSIRIS minimum measurement altitude and the tropopause altitude. Median (red circles) and percentiles (red: 1st and 99th; blue: 25th and 75th) are shown within 10° latitude bins. Altitude differences < 0 indicate that OSIRIS profiles extended below the tropopause. Altitude differences > 0 indicate that OSIRIS profiles terminated above the tropopause.

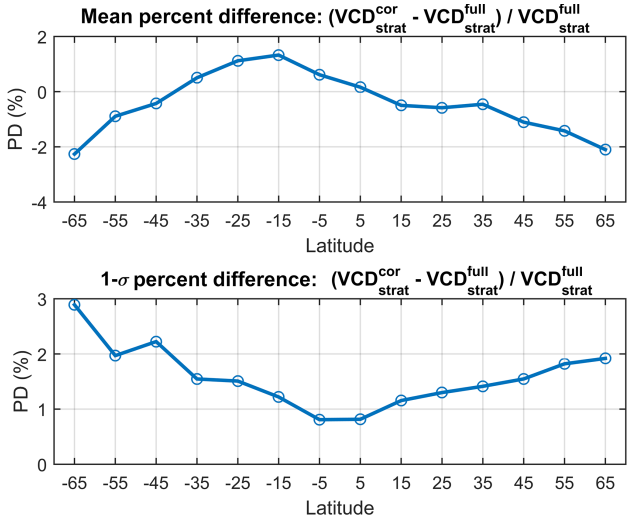

Figure 3. Effect of model scaling of OSIRIS partial VCDs for OSIRIS profiles that terminate ∼3–4 km above the thermal tropopause. **(a)** Mean and **(b)** 1 σ of percent difference of $\text{VCD}_{\text{strat}}^{\text{cor}}$ minus $\text{VCD}_{\text{strat}}^{\text{full}}$ within 10° latitude bins.

OSIRIS profiles that extended below the tropopause were used to test the effect of the VCD scaling given in Eq. (3). The results of these tests are shown in Fig. 3. $\text{VCD}_{\text{strat}}^{\text{full}}$ are the OSIRIS stratospheric VCDs calculated using the full OSIRIS profiles and Eq. (2). Data from the same OSIRIS profiles are removed for two layers above the tropopause. This

yields profiles that, on average, terminate 3.4 km above the tropopause. VCD^{cor}_{strat} is then calculated from these profiles using Eq. (3). At most latitudes, VCD^{cor}_{strat} is within 2 % of VCD^{full}_{strat}, which amounts to roughly 5×10^{13} molecules cm^{-2} of the stratospheric VCD, suggesting that the model corrections are performing well. This yields conservative estimates because most OSIRIS profiles used in this analysis extend closer to the tropopause, as shown in Fig. 2. However, it should be noted that there is a sampling bias in these tests as OSIRIS profiles that extend below the tropopause are more often available for higher tropopauses.

3.3 Calculation of gridded stratospheric VCD maps

For interpolation to OMI measurements (latitude, longitude, date, local time), daily sets of OSIRIS VCD maps were created for hourly local times, ranging from 0 to 23 h. Note that the hourly local time resolution of these maps is sufficient for interpolation to OMI NO_2 measurements because for this study, OMI measurements are used for SZA $< 75°$ when NO_2 is not varying rapidly with local time.

In order to calculate these maps, OSIRIS profiles for the time period of interest were selected. Profiles for 65° S to 65° N were used to produce VCD maps that were reliable for 60° S to 60° N, the latitude range over which OmO is calculated. These profiles were scaled to the 0–23 h local time grid using the photochemical box model (see Sect. 3.1) and stratospheric VCDs were calculated from these profiles (see Sect. 3.2).

For each local time, a filtering function was applied to the stratospheric VCDs in order to ensure a smooth field and account for irregular sampling. At each point on the regular grid, a vector of weights is calculated based on the distances between the grid point and the sparse VCD data points (i, j). The weight (w_{ij}) for a given sparse VCD data point is then calculated from the distances between the regular grid point to the sparse point in latitude $(\Delta\varphi_{ij})$ and longitude $(\Delta\lambda_{ij})$ using the following equation:

$$w_{ij} = e^{-\left(\frac{\Delta\varphi_{ij}^2}{2\sigma_\varphi^2}+\frac{\Delta\lambda_{ij}^2}{2\sigma_\lambda^2}\right)}, \quad (5)$$

where σ_φ and σ_λ are standard deviations in the Gaussian weighting, selected as discussed below. For each regular grid point, if the sum of the weight vector over all sparse VCD data points is < 1, the grid point is left empty. Otherwise, the value at the grid point is the mean of the sparse VCDs, weighted by the weighting factors. This essentially smooths the data to a finer grid; a 1° latitude and 1° longitude grid was used here.

Various combinations of Gaussian weighting standard deviations and time averaging windows (1-day, 2-day, 3-day, and 5-day) were tested. A 3-day averaging window was selected, i.e., each daily map includes measurements from the given date, the previous day, and the next day. Standard deviations for the Gaussian weighting of 6° in latitude and 10° longitude were chosen, reflecting the spatial coverage of OSIRIS measurements. These settings yield good spatial coverage in the stratospheric maps, while providing reasonable resolution of features in the VCDs. Due to the averaging and smoothing of the data, rapid changes or sharp spatial gradients in NO_2, for example when vortex remnants reach midlatitudes, may be smoothed out. This is a limitation of OSIRIS sampling.

Figure 4 shows examples of the OSIRIS VCD maps for 4 March and 21 June 2008 at the approximate OSIRIS and OMI measurement times. Note that, as described above, each of these maps is made up using 3 days of OSIRIS data. The 4 March VCD maps have global coverage from 65° S to 65° N, the latitude range over which OSIRIS profiles were included in the analysis. The 21 June maps have limited coverage in the Southern Hemisphere. This is because OSIRIS does not measure NO_2 in the winter hemisphere. The VCD maps for 07:00 LT, the approximate OSIRIS measurement time, have lower levels of NO_2 than the VCD maps for 13:00 LT, the approximate OMI measurement time. These differences with local time are typically ~ 0.4–0.5×10^{15} molecules cm^{-2} and can locally reach values of up to $\sim 1\times10^{15}$ molecules cm^{-2}. This is consistent with the daytime rates of increase in stratospheric of NO_2 VCDs measured by Dirksen et al. (2011), using OMI and Système d'Analyse par Observations Zénithal (SAOZ) data. They found increase rates that ranged from approximately 0–4×10^{15} molecules cm^{-2} h^{-1}, depending on the latitude and time of year, which would correspond to net increases of 0–2.4×10^{15} molecules cm^{-2} for the 6 h local time difference in Fig. 4. This demonstrates the effect of the diurnal scaling of NO_2 prior to matching the OSIRIS and OMI measurements.

4 Calculation of OMI-minus-OSIRIS (OmO) tropospheric NO_2

This section describes the steps involved in creating the OmO prototype dataset, using stratospheric VCDs from OSIRIS and AMFs and VCDs from the operational OMI-SP data product, and presents comparisons of the OmO and OMI operational datasets. OSIRIS stratospheric VCD maps were interpolated to the OMI measurement date, location, and local time. The interpolated OSIRIS stratospheric VCDs were compared against OMI-SP and OMI-DOMINO stratospheric VCDs, as described in Sect. 4.1. Corrections for a known high bias in OMI SCDs are presented in Sect. 4.2. OmO tropospheric NO_2 VCDs were calculated using to the equations given in Sect. 4.3. The quality of the matching between the OMI and OSIRIS stratospheres is discussed in Sect. 4.4, and the OmO tropospheric VCDs are presented and assessed in Sect. 4.5. In Sect. 4.6, an alternate OmO-DOMINO tropospheric VCD dataset is constructed and is used to interpret the relative contributions of the data used to calculate OmO.

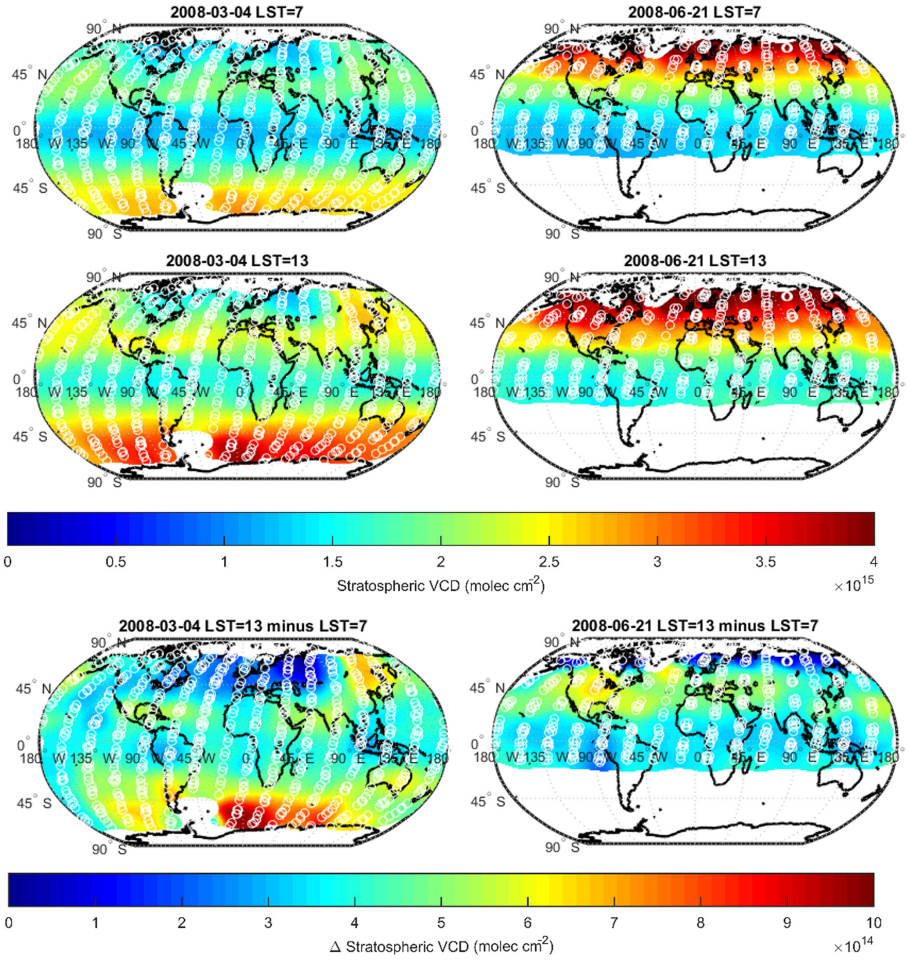

Figure 4. OSIRIS stratospheric VCD maps for 4 March 2008 (left panels) and 21 June 2008 (right panels). The maps are shown for LST = 07:00 (top panels), corresponding to the approximate OSIRIS measurement time, and LST = 13:00 (middle panels), corresponding to the approximate OMI measurement time. Difference maps for LST = 13:00 − 07:00 (bottom panels) are also shown. The white circles indicate the locations of the OSIRIS measurements used to create the maps.

4.1 Comparison of stratospheric VCDs from OMI-SP and OSIRIS

In order to obtain an OSIRIS stratospheric VCD for each OMI pixel, a linear interpolation in latitude, longitude, and local time was performed over the OSIRIS stratospheric VCD maps (see Sect. 3.3), corresponding to the OMI measurement day. Figure 5 shows the number of OMI-SP measurements that were successfully matched to the OSIRIS stratosphere using the OSIRIS gridded VCD maps. In the tropics ∼ 90 % of OMI profiles were matched to the OSIRIS stratosphere. Toward midlatitudes, this drops to ∼ 75–80 % in the Northern Hemisphere and ∼ 60–70 % in the Southern Hemisphere, because OSIRIS coverage is limited to the summer hemisphere.

Figure 6 shows a comparison between OMI-SP stratospheric VCDs and OSIRIS stratospheric VCDs, interpolated from the VCD maps. Percent differences in VCD were binned according to latitude and month for 2008. The OSIRIS VCDs are smaller than the OMI-SP VCDs for all latitudes and months, with percent differences of ∼ −20 to −30 % in the tropics and ∼ −15 to −25 % at midlatitudes. This is due to a known bias in the OMI data, as discussed in Sect. 4.2. For the most part, percent differences at a given latitude are reasonably consistent across months. This suggests that the modelled diurnal variation scale factors, which vary seasonally, are performing well. There are, however, some outliers, particularly in the winter hemisphere for April–July for 15–35° S and November–December for 25–45° N. The largest discrepancies occur toward the edge of the OSIRIS measurement range and therefore may suggest uncertainties in the OSIRIS measurements and/or photochemical model scale factors for larger SZAs ∼ 85–88° at these latitudes.

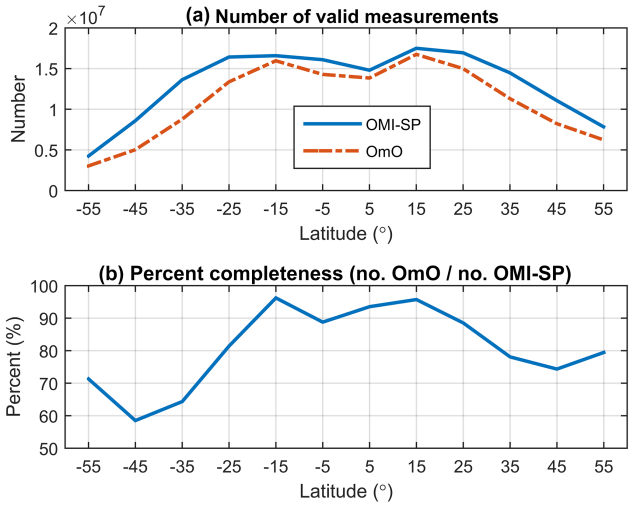

Figure 5. **(a)** Number of valid measurements for OMI-SP (blue line) and for OmO (red dashed line). **(b)** Percent completeness of the OmO-SP dataset (number of valid OmO measurements / number of valid OMI-SP measurements). Statistics were calculated in 10° latitude bins.

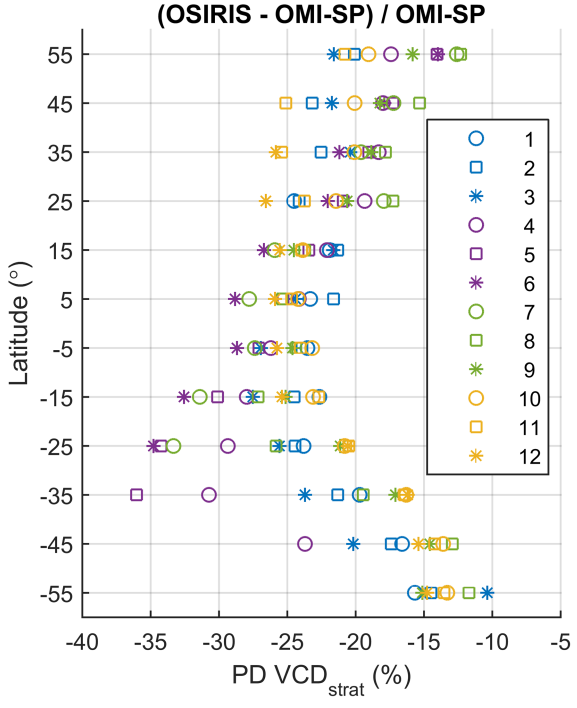

Figure 6. Mean percent difference of OSIRIS minus OMI-SP stratospheric VCDs (x axis), binned according to latitude (y axis) and month (legend). OSIRIS VCDs were interpolated from the OSIRIS gridded VCD maps (see Sect. 3.3) to the OMI measurement date, location, and local time. Filtering criteria for the OMI and OSIRIS profiles are given in Sect. 2.1 and 2.2, respectively.

Table 1. Correction factors, γ, applied to the OMI SCDs as a function of the OMI SCD. Correction factors are based on the results of Marchenko et al. (2015) and account for the high bias in the OMI SCDs.

SCD $\times 10^{16}$ molecules cm^{-2}	γ
0.5755	0.7645
0.8518	0.8049
1.2147	0.8152
1.7336	0.8475
2.3842	0.8721
3.3740	0.8912
4.4346	0.9017
5.4794	0.9082
6.4403	0.9169
7.5376	0.9218

4.2 OMI SCD bias correction

A high bias in the OMI stratospheric VCDs has been observed in comparisons with other satellite instruments (Belmonte Rivas et al., 2014) and is largely explained by a known high bias in the OMNO2A v1 SCDs of roughly 20–30 % due to issues with the spectral fitting (Marchenko et al., 2015; van Geffen et al., 2015). The OMNO2A v1 SCDs are used for both the OMI-DOMINO v2.0 and OMI-SP v2.1 retrievals. OMI tropospheric VCDs are ∼ 10–15 % smaller in polluted regions and ∼ 30 % smaller in non-polluted regions after SCDs are corrected for the spectral fitting bias (Marchenko et al., 2015).

In order to remove systematic mismatches between the OSIRIS stratospheric VCDs and the OMI measurements, the OMI total SCDs were corrected for their high bias. Marchenko et al. (2015) found that the best predictor of the relative SCD bias is the SCD itself, with small SCDs ($< 5 \times 10^{15}$ molecules cm^{-2}) having a ∼ 30 % positive bias and large SCDs ($\sim 5 \times 10^{16}$ molecules cm^{-2}) a ∼ 10 % bias. Therefore, the SCD-dependent correction factors shown in Table 1 were applied to the OMI total SCDs, using the methodology described in Sect. 4.3. Outside the range of SCDs listed in Table 1, correction factors were estimated using a linear extrapolation.

Figure 7 shows an example of bias correction factors for all OMI-SP measurements on 4 March 2008. The correction factors vary with latitude, with values closer to one at higher latitudes, where SCDs are larger. The shape of this curve is consistent with the variation in biases between the OSIRIS and OMI-SP stratospheric VCD datasets, as shown in Sect. 4.1. At northern hemispheric midlatitudes, there is a wider range of bias correction factors because a larger range of SCDs are observed in polluted regions.

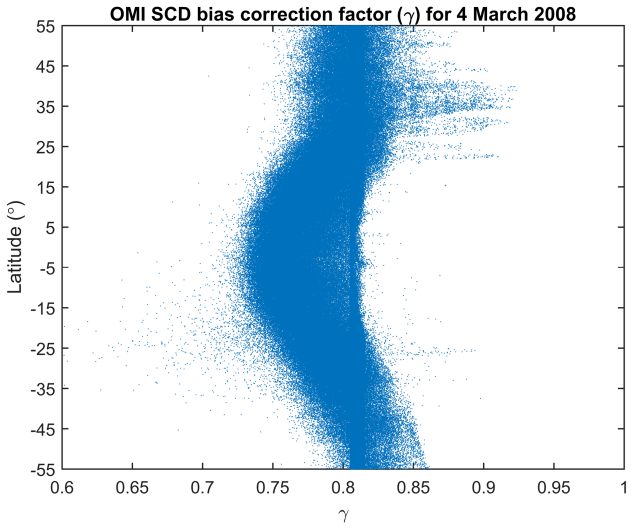

Figure 7. OMI SCD bias correction factors versus latitude for OMI-SP measurements on 4 March 2008.

4.3 Calculation of OMI-minus-OSIRIS tropospheric VCD

This section outlines the methodology used to calculate the OmO tropospheric NO_2 VCD data product. The OMI total SCD $\left(S_{\mathrm{tot}}^{\mathrm{OMI}}\right)$ can be expressed as the sum of the stratospheric and tropospheric SCDs $\left(S_{\mathrm{s}}^{\mathrm{OMI}}\right.$ and $\left.S_{\mathrm{t}}^{\mathrm{OMI}}\right)$, which are calculated from the stratospheric and tropospheric AMFs $\left(A_{\mathrm{s}}^{\mathrm{OMI}}\right.$ and $\left.A_{\mathrm{t}}^{\mathrm{OMI}}\right)$ and VCDs $\left(V_{\mathrm{s}}^{\mathrm{OMI}}\right.$ and $\left.V_{\mathrm{t}}^{\mathrm{OMI}}\right)$ as follows:

$$S_{\mathrm{tot}}^{\mathrm{OMI}} = S_{\mathrm{s}}^{\mathrm{OMI}} + S_{\mathrm{t}}^{\mathrm{OMI}} = V_{\mathrm{s}}^{\mathrm{OMI}} \cdot A_{\mathrm{s}}^{\mathrm{OMI}} + V_{\mathrm{t}}^{\mathrm{OMI}} \cdot A_{\mathrm{t}}^{\mathrm{OMI}}. \quad (6)$$

Similarly, the bias-corrected OMI SCDs can be related to the OSIRIS stratospheric VCD $\left(V_{\mathrm{s}}^{\mathrm{OSIRIS}}\right)$ and the inferred (OmO) tropospheric VCD component $\left(V_{\mathrm{t}}^{\mathrm{OmO}}\right)$, using the AMFs from the OMI operational products:

$$S_{\mathrm{tot}}^{\mathrm{OMI}} \cdot \gamma = V_{\mathrm{s}}^{\mathrm{OSIRIS}} \cdot A_{\mathrm{s}}^{\mathrm{OMI}} + V_{\mathrm{t}}^{\mathrm{OmO}} \cdot A_{\mathrm{t}}^{\mathrm{OMI}}, \quad (7)$$

where γ is the OMI SCD bias correction factor described in Sect. 4.2. Solving for the OmO VCD gives

$$V_{\mathrm{t}}^{\mathrm{OmO}} = \left(\gamma \cdot S_{\mathrm{tot}}^{\mathrm{OMI}} - V_{\mathrm{s}}^{\mathrm{OSIRIS}} \cdot A_{\mathrm{s}}^{\mathrm{OMI}}\right) / A_{\mathrm{t}}^{\mathrm{OMI}}. \quad (8)$$

An alternate form, and the one used to compute the OmO product, is obtained by combining Eqs. (6) and (8):

$$V_{\mathrm{t}}^{\mathrm{OmO}} = \gamma \cdot V_{\mathrm{t}}^{\mathrm{OMI}} + \left(\gamma \cdot V_{\mathrm{s}}^{\mathrm{OMI}} - V_{\mathrm{s}}^{\mathrm{OSIRIS}}\right) \cdot A_{\mathrm{s}}^{\mathrm{OMI}} / A_{\mathrm{t}}^{\mathrm{OMI}}. \quad (9)$$

OmO tropospheric VCDs were computed using AMFs and VCDs from the OMI-SP product. The ratio of AMFs represents the different sensitivities to NO_2 located in the troposphere and in the stratosphere. Typically, the ratio $A_{\mathrm{s}}^{\mathrm{OMI}}/A_{\mathrm{t}}^{\mathrm{OMI}}$ is greater than 1, indicating that OMI is more sensitive to NO_2 within the stratosphere. OmO was not calculated for the small number of OMI measurements for which the ratio $A_{\mathrm{s}}^{\mathrm{OMI}}/A_{\mathrm{t}}^{\mathrm{OMI}} > 15$, indicating that the OMI measurement is not very sensitive to the troposphere. For each OMI pixel, $V_{\mathrm{s}}^{\mathrm{OSIRIS}}$ was interpolated from the OSIRIS gridded VCD maps (see Sect. 4.1) and γ was interpolated to the OMI SCD (see Sect. 4.2).

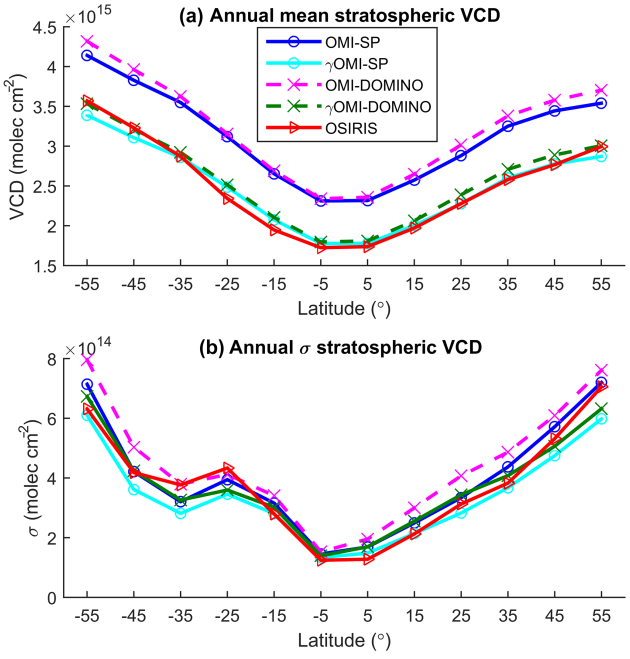

Figure 8. Annual **(a)** mean and **(b)** standard deviation of stratospheric VCDs for 2008 in 10° latitude bins for measurements with OMI tropospheric VCDs $< 0.5\times10^{15}$ molecules cm^{-2}. Stratospheric VCDs for OMI-SP (blue circles), OMI-SP scaled by γ (cyan circles), OMI-DOMINO (magenta X's), OMI-DOMINO scaled by γ (green X's), and OSIRIS VCD maps interpolated to the OMI measurement time/location (red triangles) are shown. Mean and standard deviation are calculated over individual OMI measurements for the entire year.

4.4 Matching of OSIRIS and OMI stratospheres

Over unpolluted regions, the OmO tropospheric VCDs should be small and, subsequently, the $\left(\gamma \cdot V_{\mathrm{s}}^{\mathrm{OMI}} - V_{\mathrm{s}}^{\mathrm{OSIRIS}}\right)$ term in Eq. (9) should also be small. Therefore, the matching of the OSIRIS and OMI stratospheres can be assessed by comparing OSIRIS stratospheric VCDs with OMI VCDs scaled with γ, over unpolluted regions. Figure 8 shows annual average stratospheric VCDs for OMI-SP, OMI-DOMINO, and OSIRIS, binned by latitude over unpolluted regions (OMI tropospheric VCDs $< 0.5 \times 10^{15}$ molecules cm^{-2}). Annual average OMI-SP and OMI-DOMINO stratospheric VCDs are larger than OSIRIS VCDs by $\sim 0.6 \times 10^{15}$ molecules cm^{-2} for all latitudes. When OMI-SP and OMI-DOMINO stratospheric VCDs are

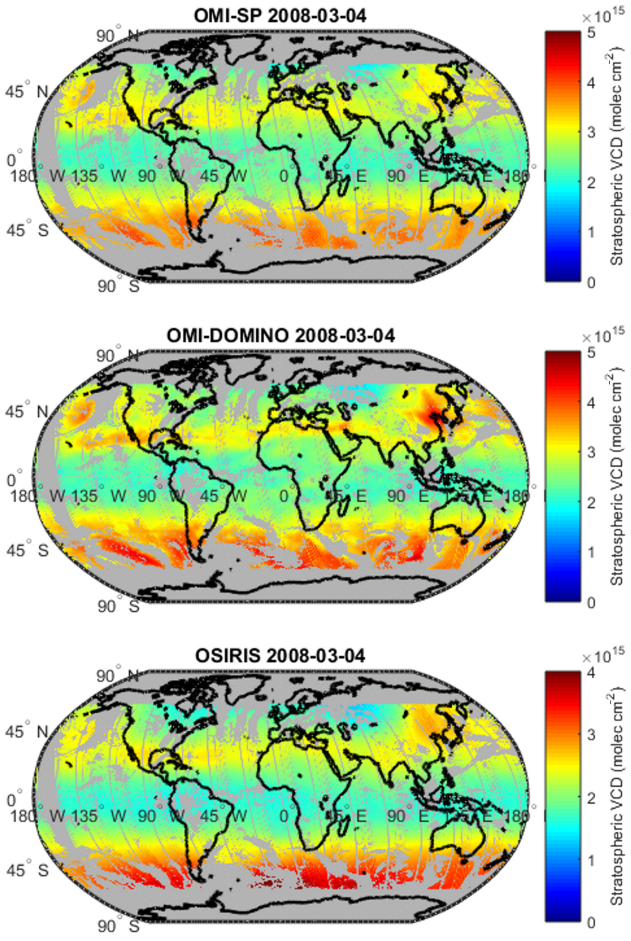

Figure 9. Maps of stratospheric VCDs for 4 March 2008 for OMI-SP (top), OMI-DOMINO (middle), and OSIRIS interpolated to the location of OMI measurements (bottom). Note that different colour scales are used for the OMI and OSIRIS VCDs.

scaled with γ, agreement with OSIRIS is to within 0.2×10^{15} molecules cm^{-2} at all latitudes. This suggests that the OMI and OSIRIS stratospheres are well matched. Standard deviations over the year of the individual γ-scaled OMI VCDs are similar to OSIRIS VCDs at most latitudes. At 25, 35° S, and 55° N, the standard deviation in the OSIRIS VCDs is larger than the standard deviation in the OMI-SP or OMI-DOMINO VCDs.

OMI-SP, OMI-DOMINO, and OSIRIS stratospheric VCD maps are shown for 4 March 2008 in Fig. 9. The OMI VCDs are larger than the OSIRIS VCDs due to the high bias in the OMI SCDs. There is somewhat less structure in the OSIRIS VCDs than in the OMI VCDs. For example, OMI-DOMINO and OMI-SP stratospheric VCDs are enhanced across the northern hemispheric Pacific and Mexico, but enhancements are not as strong in the OSIRIS data. There is a large maximum in the OMI-DOMINO stratospheric VCDs over eastern China and Korea, which is not apparent in the OMI-SP or OSIRIS VCDs. These features across the northern hemispheric Pacific and Mexico and over eastern China and Korea all persist in the OMI data over the OSIRIS 3-day sampling period and cover a large enough area that they could be resolved, although perhaps somewhat distorted, by the OSIRIS VCD maps. Therefore, these local differences between the OSIRIS and OMI stratospheric VCDs cannot be attributed to the smoothing and averaging of the OSIRIS measurements.

4.5 OmO tropospheric VCDs

Figure 10 shows the OmO tropospheric VCDs, also for 4 March 2008. At most locations, OmO VCDs are similar to the OMI-SP and OMI-DOMINO VCDs, with a few notable differences. OmO VCDs are larger than OMI-SP and OMI-DOMINO VCDs over the northern hemispheric Pacific and Mexico, which is consistent with the differences in the observed features in the stratospheric VCDs. OmO VCDs are larger than OMI-DOMINO VCDs over eastern China and Korea, as OmO effectively redistributes NO_2 from the stratosphere into the troposphere through the second term in Eq. (9). Over much of India and China, OmO VCDs are smaller than the OMI-SP VCDs.

Maps of annual average comparisons between OmO, OMI-SP, and OMI-DOMINO tropospheric NO_2 are shown in Fig. 11. Over unpolluted regions, differences between OmO and the operational OMI data products are fairly small, suggesting that the matching of the OSIRIS and OMI stratospheres was effective. OmO has less NO_2 than OMI-SP and OMI-DOMINO over polluted regions such as the eastern United States, Europe, and eastern China. This is expected as the OMI-SP and OMI-DOMINO tropospheric VCDs are biased high by ∼ 10–15 % over polluted regions due to the bias in the SCDs (Marchenko et al., 2015). Over Korea, both the OMI-SP and OmO VCDs are larger than the OMI-DOMINO VCDs. At southern hemispheric midlatitudes, both the OmO and OMI-DOMINO VCDs are biased low relative to OMI-SP VCDs. Overall, the differences between the OmO VCDs and the operational OMI data products are within the range of the differences between the two operational OMI data products.

Tropospheric VCDs over the Pacific Ocean can be used to assess the quality of the stratosphere–troposphere separation because tropospheric VCDs are expected to be near background levels. Figure 5 from Hilboll et al. (2013) shows climatological monthly mean tropospheric VCDs over the Pacific (180–150° W) binned according to month and latitude over 1998–2007, as calculated from Oslo CTM2 model simulations (Søvde et al., 2008). At most latitudes, tropospheric VCDs are $< 3 \times 10^{14}$ molecules cm^{-2} according to the model results. For northern hemispheric midlatitudes, tropospheric VCDs are somewhat larger, ranging from ∼ 2 to 7×10^{14} molecules cm^{-2}, with the largest values at ∼ 55° N in winter months.

Figure 12 shows monthly mean tropospheric VCDs from OMI-SP, OMI-DOMINO, and OmO over the Pacific (180–

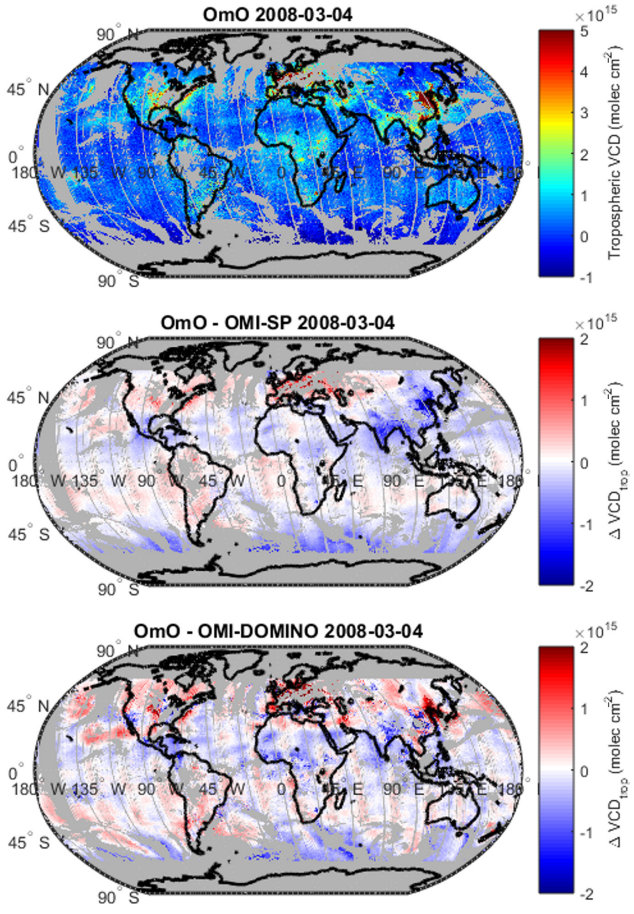

Figure 10. Maps of tropospheric VCDs for 4 March 2008 for OmO (top), the difference between OmO and OMI-SP (middle), and the difference between OmO and OMI-DOMINO (bottom).

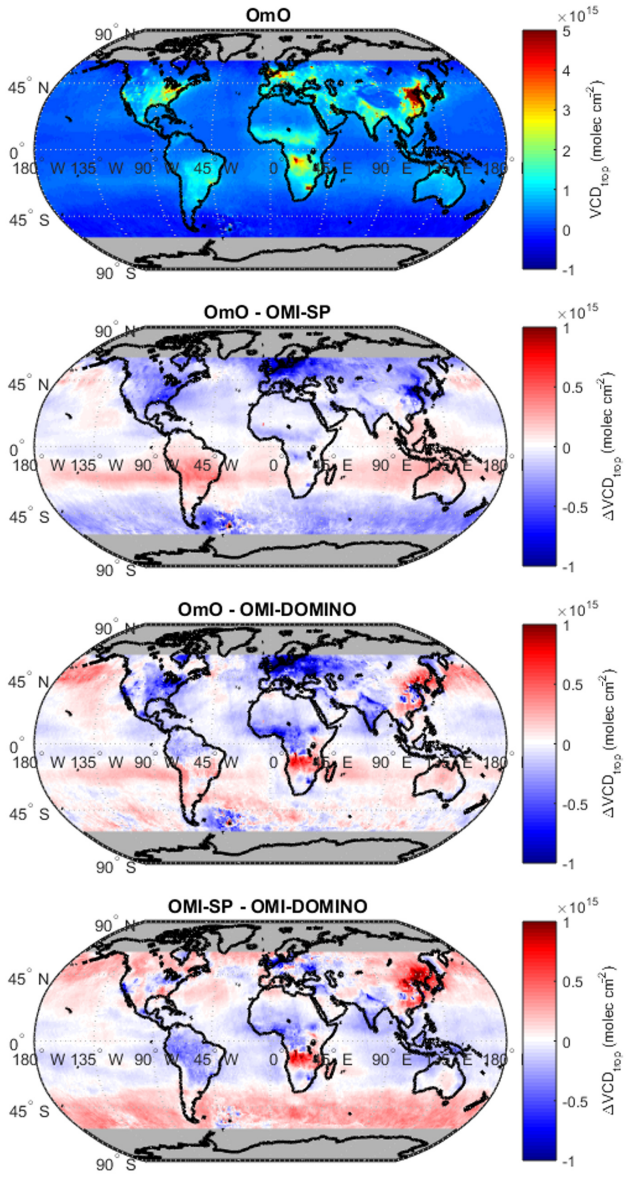

Figure 11. Maps of annual average (top) OmO tropospheric VCDs and differences between tropospheric VCDs for (top-middle) OmO minus OMI-SP, (bottom-middle) OmO minus OMI-DOMINO, and (bottom) OMI-SP minus OMI-DOMINO. Maps are averaged on a $1 \times 1°$ grid.

150° W). The OMI-SP VCDs vary less with latitude and have no mean negative values, unlike the OMI-DOMINO and OmO VCDs. This is expected as the OMI-SP stratosphere–troposphere separation uses measurements over unpolluted regions, including the Pacific, to estimate stratospheric NO_2. In the tropics, average VCDs from all three datasets are $< 3 \times 10^{14}$ molecules cm^{-2}, which is consistent with background levels. At northern hemispheric midlatitudes, OmO mean VCDs increase slightly, ranging from $\sim 2.5 \times 10^{14}$ to $\sim 5 \times 10^{14}$ molecules cm^{-2}. This is different from the OMI-SP and OMI-DOMINO VCDs, which mostly remain $< 3 \times 10^{14}$ molecules cm^{-2}, but is consistent with the Oslo CTM2 model simulations. At 55° N, both OmO and DOMINO mean VCDs are close to 0 molecules cm^{-2}. In the Southern Hemisphere, VCDs for all three datasets decrease with latitude, reaching values near 0 molecules cm^{-2} in the OMI-SP and negative values in the OMI-DOMINO and OmO datasets at 45 and 55° S. There are some large outliers in the OmO VCDs for April–July in the Southern Hemisphere, suggesting a positive bias in the OmO dataset, likely because the OMI and OSIRIS stratospheres were not well matched (see Sect. 4.1). This is consistent with the observed differences between OSIRIS and OMI-SP stratospheric VCDs for the same latitudes and months. The standard deviations of the individual OmO and DOMINO tropospheric VCDs over each month are also shown. All three datasets have smaller standard deviations in the tropics and larger standard deviations toward midlatitudes in both hemispheres. For the most part, the variability in the OmO VCDs is slightly smaller than the variability in the OMI-DOMINO VCDs.

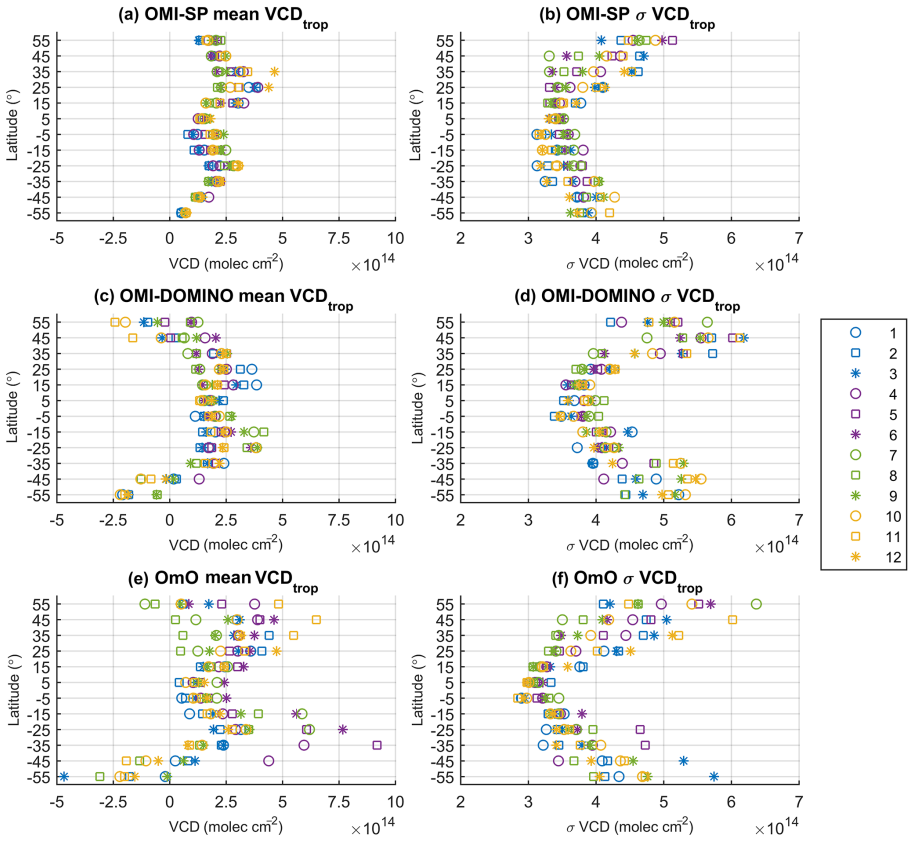

Figure 12. Mean and standard deviation of VCDs in the Pacific (150–180° W), calculated monthly (legend) in 10° latitude bins. **(a)** OMI-SP mean VCD, **(b)** OMI-SP standard deviation of VCD, **(c)** OMI-DOMINO mean VCD, **(d)** OMI-DOMINO standard deviation of VCD, **(e)** OmO mean VCD, and **(f)** OmO standard deviation of VCD.

4.6 Alternate OmO-DOMINO tropospheric VCDs

The OmO dataset is affected by the scaling of OSIRIS stratospheric VCDs to the OMI local times, the OMI SCD bias correction factor, the difference between the OMI and OSIRIS stratospheres, and the choice of the OMI version of AMFs and VCDs (see Eq. 9). In order to gain some insight into the impact of these various terms in the OmO calculation, an alternate OmO-DOMINO dataset was constructed using the OMI-DOMINO VCDs and AMFs (Fig. 13). Over unpolluted regions, the OmO and OmO-DOMINO VCDs are very similar. Over polluted areas, the OmO-DOMINO VCDs are somewhat larger than the OmO VCDs. However, these differences are smaller in magnitude than the differences between the two OmO products and the operational OMI data products (Figs. 11 and 13). The relative contribution of the various terms in Eq. (9) to the OmO and OmO-DOMINO datasets are discussed in the paragraphs below.

In order to match the OMI and OSIRIS stratospheres, both the OSIRIS and OMI datasets were scaled prior to stratospheric subtraction. The OSIRIS stratospheric VCDs, measured in the morning, were scaled to the OMI afternoon local time using a photochemical model, typically increasing the OSIRIS stratospheric VCDs by $\sim 0.5 \times 10^{15}$ molecules cm^{-2}. The OMI SCD bias correction factor was applied to OMI SCDs before creating the OmO and OmO-DOMINO datasets. This correction factor is required in order to properly match the OMI and OSIRIS stratospheres, for both the OMI-SP and OMI-DOMINO datasets (Fig. 8). Without the correction factor, both the OmO and OmO-DOMINO tropospheric VCDs would be very large ($\sim 1 \times 10^{15}$ molecules cm^{-2}) over the unpolluted Pacific Ocean. After the application of the diurnal variation scaling and OMI SCD bias correction, the OMI-SP, OMI-DOMINO, and OSIRIS stratospheres VCDs agree to within $\sim 0.2 \times 10^{15}$ molecules cm^{-2} on an annual average basis over unpolluted areas (Fig. 8). Furthermore, good overall matching of the stratosphere is demonstrated by the OmO tropospheric VCDs over the Pacific Ocean (Fig. 12). At specific locations/times, the differences in the stratospheric VCDs can be much larger (Fig. 9), but this is difficult to quantify because of the role of the OMI SCD bias correction, which varies according to the magnitude of the SCD. Therefore, the scaling of OSIRIS to the OMI local time and the OMI SCD bias correction play similar and important roles for the both the OmO and OmO-DOMINO datasets.

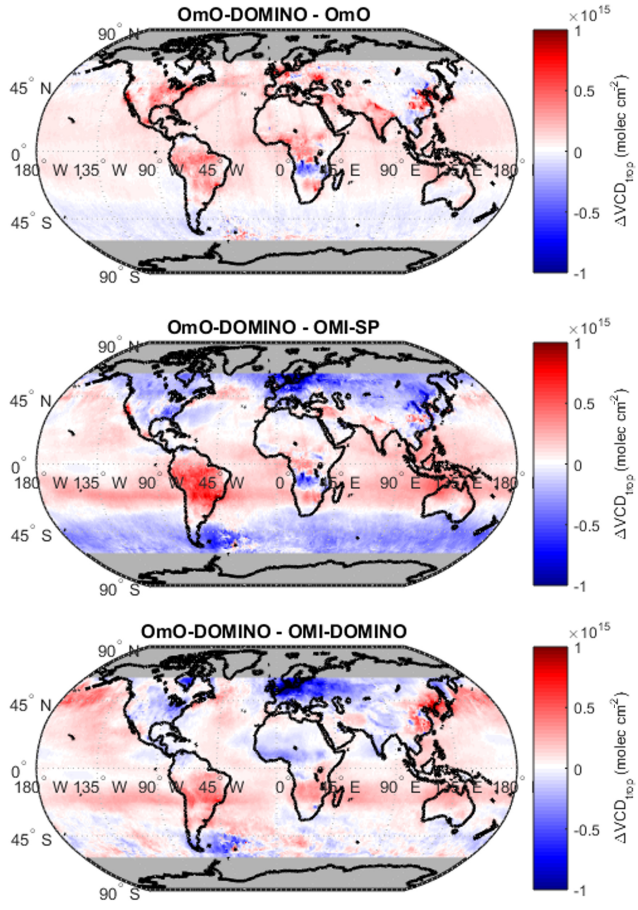

Figure 13. Maps of differences between OmO-DOMINO and (top) OmO, (middle) OMI-SP, and (bottom) OMI-DOMINO annual average tropospheric VCDs. Map is averaged on a $1 \times 1°$ grid.

The OmO VCDs also depend on the ratio of AMFs (A_s/A_t), which scales the difference between the OSIRIS and OMI stratospheric VCDs. Over unpolluted regions, this ratio is ~ 1.25 and is nearly identical for both OMI-SP and OMI-DOMINO. Over polluted regions, the ratio is larger, reaching annual averages of ~ 3–4 in some locations. Therefore, differences between OSIRIS and OMI stratospheric VCDs are amplified over polluted areas through the dependence on A_s/A_t in Eq. (9). Over polluted areas, A_s/A_t is somewhat smaller for OMI-SP than for OMI-DOMINO, though the relationship is complicated because Eq. (9) also depends on the OMI tropospheric VCDs, which also differ between the two operational OMI products, primarily over polluted regions (Fig. 11). This is consistent with the observed differences between the OmO and OmO-DOMINO datasets, which are largest over polluted areas.

Overall, these tests suggest that the stratospheric matching between OSIRIS and OMI has a larger influence on the OmO dataset than the choice of OMI AMFs. The stratospheric matching currently depends on the OSIRIS and operational OMI stratospheric VCDs, as well as the OMI SCD bias correction. Considering the complex manner in which biases in SCDs are transferred into the OMI-SP and OMI-DOMINO stratospheric VCD, which can then affect unconstrained (polluted) locations, it is impossible at this time to disentangle the impact of the SCD bias from the larger issue of how well each method of stratospheric removal performs. Therefore, the stratospheric matching between OSIRIS and OMI will be better understood once bias-corrected OMI SCDs are available.

5 Summary and future applications

The technique of matching nadir- and limb-viewing satellite retrievals to quantify tropospheric NO_2 is explored in this work using OMI nadir measurements and OSIRIS limb measurements to create the OmO tropospheric NO_2 dataset. As nadir-viewing instruments cannot resolve NO_2 in the vertical, additional information or assumptions based on unpolluted regions are required to determine quantities in the upper and lower atmospheric regions. Currently, there are two operational products for OMI, which estimate stratospheric NO_2 using different methods. The OMI-DOMINO product assimilates OMI SCDs into the TM4 model and then subtracts modelled stratospheric NO_2. The OMI-SP dataset estimates stratospheric VCDs for locations with background levels of tropospheric NO_2 and then uses an extrapolation technique to infer stratospheric VCDs across the globe.

The new OmO tropospheric NO_2 dataset uses information from OSIRIS profile measurements in order to estimate the stratospheric contribution to OMI SCD measurements. OSIRIS NO_2 stratospheric VCDs were found to agree to within 0.25×10^{15} molecules cm^{-2} of the SCIAMACHY, HIRDLS, and MIPAS limb instruments for most latitudes and seasons (Appendix A). OSIRIS profile measurements of stratospheric NO_2 were scaled to a range of local times using a photochemical model. Stratospheric VCDs were calculated and were gridded onto daily maps of stratospheric NO_2 for various local times. The OSIRIS VCD maps were averaged over a 3-day window in order to gain sufficient coverage from the OSIRIS measurements, which could smooth out rapid variations in stratospheric NO_2, such as vortex intrusions. For each OMI measurement, the OSIRIS VCD maps were interpolated to the latitude, longitude, and local time of the OMI measurement. Then the OSIRIS stratospheric VCD and OMI-SP VCDs and AMFs were used to calculate the OmO product for 60° S–60° N. In order to match the OSIRIS and OMI data products, corrections for a known bias in OMI SCDs were applied based on the findings of Marchenko et al. (2015). After accounting for a bias in the OMI SCDs, the OSIRIS and OMI annual average stratospheric VCDs agree to within 0.2×10^{15} molecules cm^{-2} between 60° S and 60° N. Therefore, no additional corrections were applied to the data.

The OmO tropospheric VCDs reproduced the broad features of the OMI-SP and OMI-DOMINO tropospheric VCDs. Furthermore, over the Pacific Ocean, the OmO VCDs were consistent with background levels of NO_2 at most latitudes, suggesting that, overall, the stratospheric NO_2 signal has been successfully removed using the OSIRIS dataset. There are high biases in the OmO dataset for $\sim$20–40° S in April–July, which are consistent with observed systematic differences between the OSIRIS and OMI stratospheric VCDs for these latitudes and months. Despite this, the matching of the OSIRIS and OMI stratospheres is very good given the rudimentary nature of the OMI SCD-bias correction. No corrections were applied to account for biases between the OSIRIS and OMI datasets. This differs from the technique of Hilboll et al. (2013), who matched SCIAMACHY limb and nadir measurements through daily corrections based on the comparisons over the Pacific Ocean. At present, errors remaining after the simple OMI bias-correction cannot be separated from those in OSIRIS stratospheric VCD. As such a more quantitative assessment of the potential of this approach can be made only once the next version of OMI SCDs is available.

The results of this study show preliminary success in the compatibility of limb and nadir measurements taken at different local times in a simpler framework. This technique could be improved by better accounting for biases between the OMI and OSIRIS datasets. For example, in a full analysis, limb-measured stratospheric NO_2 and nadir-measured columns could be assimilated together in a chemical transport model to estimate stratospheric NO_2.

This work underlines the challenge associated with matching polar orbiting, limb-viewing instruments with future geostationary nadir-viewing instruments as the measurements occur at many local solar times. By the end of the decade, three instruments, each on board a geostationary satellite will measure NO_2 in the nadir-viewing geometry: Sentinel-4 (Ingmann et al., 2012) with coverage over Europe, TEMPO (Zoogman et al., 2016) with coverage over North America, and GEMS (Kim, 2012) with coverage over eastern Asia. While this study demonstrates that limb and nadir measurements could be matched to retrieve tropospheric NO_2, there are currently no planned limb instruments to overlap with these geostationary missions. OSIRIS is well beyond its expected lifetime and there are no planned satellites that can measure stratospheric NO_2 beyond 2017, when the Stratospheric Aerosol and Gas Experiment III (SAGE III) on the International Space Station (ISS) reaches the end of its 1-year design lifetime.

6 Data availability

OSIRIS data are available at http://odin-osiris.usask.ca. OMI-SP data are available at http://daac.gsfc.nasa.gov/. OMI-DOMINO data are available at http://www.temis.nl.

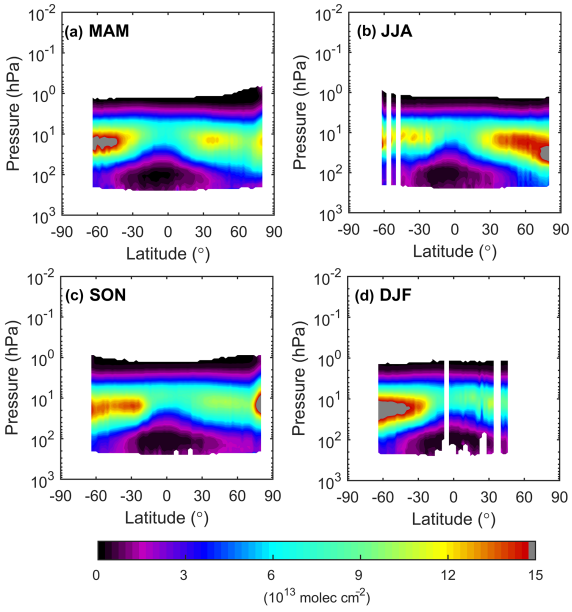

Figure A1. OSIRIS seasonal mean NO_2 partial column profiles for 1 February 2005–31 January 2008 in 2° latitude bins for **(a)** March–April–May (MAM), **(b)** June–July–August (JJA), **(c)** September–October–November (SON), and **(d)** December–January–February (DJF).

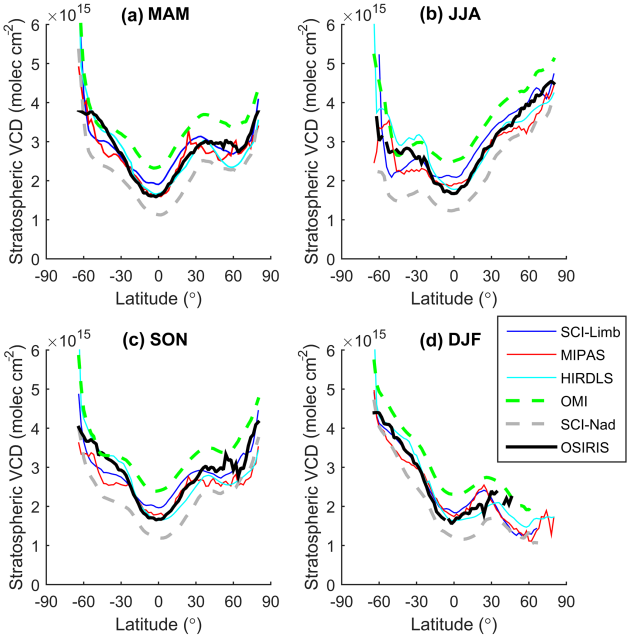

Figure A2. Seasonal averages of stratospheric NO_2 VCDs for 1 February 2005–31 January 2008 in 2° latitude bins for **(a)** March–April–May (MAM), **(b)** June–July–August (JJA), **(c)** September–October–November (SON), and **(d)** December–January–February (DJF). SCIAMACHY-limb (blue line), MIPAS (red line), HIRDLS (cyan line), OMI (green dashed line), SCIAMACHY-nadir (grey dashed line), and OSIRIS (thick black line) are all shown. Figure is adapted from Belmonte Rivas et al. (2014).

Appendix A: Comparison of OSIRIS NO_2 to other satellite instruments

In order to assess the OSIRIS v5 NO_2 product, OSIRIS data for 2005–2007 were compared against the results of Belmonte Rivas et al. (2014). The study included limb satellite measurements from MIPAS (IMK-IAA version 4.0; Funke et al., 2005), HIRDLS (version 7; Gille et al., 2012), and SCIAMACHY (v3.1; Bauer et al., 2012), as well as satellite nadir measurements from OMI (KNMI DOMINO version 2.0, Boersma et al., 2004, 2011) and SCIAMACHY (KNMI-BIRA TM4NO2A version 2.3; Boersma et al., 2004). Belmonte Rivas et al. (2014) found that the limb stratospheric VCDs from SCIAMACHY-limb, MIPAS, and HIRDLS agree to within 0.25×10^{15} molecules cm^{-2}, which is better than 10 %, when all observations are adjusted to the HIRDLS local time. Nadir SCIAMACHY and OMI stratospheric VCDs are biased relative to the limb instruments by −20 % (-0.5×10^{15} molecules cm^{-2}) and +20 % (0.6×10^{15} molecules cm^{-2}), respectively.

OSIRIS profiles were averaged using the methodology of Belmonte Rivas et al. (2014). OSIRIS profiles were scaled to the HRDLS local time of ∼ 15:30 LT (Fig. 3 of Belmonte Rivas et al., 2014), using the photochemical model described in Sect. 2.3 and the methodology described in Sect. 3.1. The photochemical model runs for the 2005–2007 OSIRIS profiles presented here use the settings described by Brohede et al. (2008). Volume mixing ratio (VMR) profiles were averaged daily in 2° latitude bins from 64° S to 80° N. Partial column profiles $n_v(z_i)$ were calculated from the VMRs (V) using

$$n_{v(z_i)} = 10 \cdot N_A/(g \cdot M_{air}) \cdot 0.5 \cdot (V_{i+1} + V_i) \cdot (p_{i+1} - p_i), \quad \text{(A1)}$$

where N_A is Avogadro's constant (6.022×10^{23} molecules mole^{-1}), g is the Earth's gravity (9.80 m s^{-2}), and M_{air} is the molar mass of air (28.97 g mole^{-1}). The pressure increments in hPa were $p_i = 1000 \times 10^{-i/24}$ for $i = 0$–120. Belmonte Rivas et al. (2014) imposed collocation criteria as well as some smoothing, which were not included here. Therefore, the comparisons presented here are similar to the figures of Belmonte Rivas et al. (2014), but not identical.

Figure A1 shows OSIRIS partial column profiles versus latitude averaged over four seasons for 1 February 2005–31 January 2008. The OSIRIS profiles reproduce the altitude variation and seasonality of the other datasets, shown in Fig. 6 of Belmonte Rivas et al. (2014) over the same altitude range. Stratospheric VCDs were calculated from the OSIRIS partial column profiles from the top altitude of the available measurements to 287 hPa. OSIRIS stratospheric VCDs are shown in Fig. A2, alongside SCIAMACHY-limb, MIPAS, HIRDLS, SCIAMACHY-nadir, and OMI measure-

ments. This figure is similar to Fig. 8 of Belmonte Rivas et al. (2014). OSIRIS stratospheric VCDs are within 0.25×10^{15} molecules cm^{-2} of the other limb instruments (SCIAMACHY-limb, MIPAS, and HIRDLS) for most latitudes and seasons. However, there are some localised differences between all four limb instruments of $\sim 0.5 \times 10^{15}$ molecules cm^{-2}, especially toward higher latitudes. These biases are not due to broad differences in sampling, as similar differences are also observed in Fig. 8 of Belmonte Rivas et al. (2014), where collocation criteria were imposed. Therefore the localised differences between the limb instruments are related to uncertainties in the measurements or the local time corrections.

Acknowledgements. This work was supported by the Natural Sciences and Engineering Research Council (Canada) and the Canadian Space Agency. Odin is a Swedish-led satellite project funded jointly by Sweden (SNSB), Canada (CSA), France (CNES), and Finland (Tekes). The authors thank David Plummer for the provision of climatological fields from the Canadian Middle Atmosphere Model. Thanks to Sergey Marchenko for providing the OMI SCD bias correction factors. Thank you also to Chris Roth for help with the OSIRIS database.

Edited by: V. Sofieva
Reviewed by: two anonymous referees

References

Bauer, R., Rozanov, A., McLinden, C. A., Gordley, L. L., Lotz, W., Russell III, J. M., Walker, K. A., Zawodny, J. M., Ladstätter-Weißenmayer, A., Bovensmann, H., and Burrows, J. P.: Validation of SCIAMACHY limb NO_2 profiles using solar occultation measurements, Atmos. Meas. Tech., 5, 1059–1084, doi:10.5194/amt-5-1059-2012, 2012.

Beirle, S., Kühl, S., Puķīte, J., and Wagner, T.: Retrieval of tropospheric column densities of NO_2 from combined SCIAMACHY nadir/limb measurements, Atmos. Meas. Tech., 3, 283–299, doi:10.5194/amt-3-283-2010, 2010.

Belmonte Rivas, M., Veefkind, P., Boersma, F., Levelt, P., Eskes, H., and Gille, J.: Intercomparison of daytime stratospheric NO_2 satellite retrievals and model simulations, Atmos. Meas. Tech., 7, 2203–2225, doi:10.5194/amt-7-2203-2014, 2014.

Belmonte Rivas, M., Veefkind, P., Eskes, H., and Levelt, P.: OMI tropospheric NO_2 profiles from cloud slicing: constraints on surface emissions, convective transport and lightning NO_x, Atmos. Chem. Phys., 15, 13519–13553, doi:10.5194/acp-15-13519-2015, 2015.

Boersma, K. F., Eskes, H. J., and Brinksma, E. J.: Error analysis for tropospheric NO_2 retrieval from space, J. Geophys. Res., 109, D04311, doi:10.1029/2003JD003962, 2004.

Boersma, K. F., Eskes, H. J., Veefkind, J. P., Brinksma, E. J., van der A, R. J., Sneep, M., van den Oord, G. H. J., Levelt, P. F., Stammes, P., Gleason, J. F., and Bucsela, E. J.: Near-real time retrieval of tropospheric NO_2 from OMI, Atmos. Chem. Phys., 7, 2103–2118, doi:10.5194/acp-7-2103-2007, 2007.

Boersma, K. F., Eskes, H. J., Dirksen, R. J., van der A, R. J., Veefkind, J. P., Stammes, P., Huijnen, V., Kleipool, Q. L., Sneep, M., Claas, J., Leitão, J., Richter, A., Zhou, Y., and Brunner, D.: An improved tropospheric NO_2 column retrieval algorithm for the Ozone Monitoring Instrument, Atmos. Meas. Tech., 4, 1905–1928, doi:10.5194/amt-4-1905-2011, 2011.

Bovensmann, H., Burrows, J. P., Buchwitz, M., Frerick, J., Noël, S., Rozanov, V. V., Chance, K. V., and Goede, A. P. H.: SCIAMACHY: Mission Objectives and Measurement Modes, J. Atmos. Sci., 56, 127–150, doi:10.1175/1520-0469(1999)056<0127:SMOAMM>2.0.CO;2, 1999.

Brohede, S., McLinden, C. A., Urban, J., Haley, C. S., Jonsson, A. I., and Murtagh, D.: Odin stratospheric proxy NO_y measurements and climatology, Atmos. Chem. Phys., 8, 5731–5754, doi:10.5194/acp-8-5731-2008, 2008.

Brohede, S. M., Haley, C. S., McLinden, C. A., Sioris, C. E., Murtagh, D. P., Petelina, S. V., Llewellyn, E. J., Bazureau, A., Goutail, F., Randall, C. E., Lumpe, J. D., Taha, G., Thomasson, L. W., and Gordley, L. L.: Validation of Odin/OSIRIS stratospheric NO_2 profiles, J. Geophys. Res.-Atmos., 112, D07310, doi:10.1029/2006JD007586, 2007.

Bucsela, E. J., Celarier, E. A., Wenig, M. O., Gleason, J. F., Veefkind, J. P., Boersma, K. F., and Brinksma, E. J.: Algorithm for NO_2 vertical column retrieval from the ozone monitoring instrument, IEEE T. Geosci. Remote Sens., 44, 1245–1258, doi:10.1109/TGRS.2005.863715, 2006.

Bucsela, E. J., Krotkov, N. A., Celarier, E. A., Lamsal, L. N., Swartz, W. H., Bhartia, P. K., Boersma, K. F., Veefkind, J. P., Gleason, J. F., and Pickering, K. E.: A new stratospheric and tropospheric NO_2 retrieval algorithm for nadir-viewing satellite instruments: applications to OMI, Atmos. Meas. Tech., 6, 2607–2626, doi:10.5194/amt-6-2607-2013, 2013.

Burrows, J. P., Weber, M., Buchwitz, M., Rozanov, V., Ladstätter-Weißenmayer, A., Richter, A., DeBeek, R., Hoogen, R., Bramstedt, K., Eichmann, K.-U., Eisinger, M., and Perner, D.: The Global Ozone Monitoring Experiment (GOME): Mission, instrument concept, and first scientific results, J. Atmos. Sci., 56, 151–175, doi:10.1175/1520-0469(1999)056<0151:TGOMEG>2.0.CO;2, 1999.

Callies, J., Corpaccioli, E., Eisinger, M., Hahne, A., and Lefebvre, A.: GOME-2 – Metop's second-generation sensor for operational ozone monitoring, ESA Bull. Sp. Agency, 102, 28–36, 2000.

Chance, K. V. and Spurr, R. D.: Ring effect studies: Rayleigh scattering, including molecular parameters for rotational Raman scattering, and the Fraunhofer spectrum, Appl. Opt., 36, 5224–5230, doi:10.1364/AO.36.005224, 1997.

Choi, S., Joiner, J., Choi, Y., Duncan, B. N., Vasilkov, A., Krotkov, N., and Bucsela, E.: First estimates of global free-tropospheric NO_2 abundances derived using a cloud-slicing technique applied to satellite observations from the Aura Ozone Monitoring Instrument (OMI), Atmos. Chem. Phys., 14, 10565–10588, doi:10.5194/acp-14-10565-2014, 2014.

Degenstein, D. A., Bourassa, A. E., Roth, C. Z., and Llewellyn, E. J.: Limb scatter ozone retrieval from 10 to 60 km using a multiplicative algebraic reconstruction technique, Atmos. Chem. Phys., 9, 6521–6529, doi:10.5194/acp-9-6521-2009, 2009.

Dirksen, R. J., Boersma, K. F., Eskes, H. J., Ionov, D. V., Bucsela, E. J., Levelt, P. F., and Kelder, H. M.: Evaluation of stratospheric NO_2 retrieved from the Ozone Monitoring Instrument: Intercomparison, diurnal cycle, and trending, J. Geophys. Res.-Atmos., 116, D08305, doi:10.1029/2010JD014943, 2011.

Duncan, B. N., Lamsal, L. N., Thompson, A. M., Yoshida, Y., Lu, Z., Streets, D. G., Hurwitz, M. M., and Pickering, K. E.: A space-based, high-resolution view of notable changes in urban NO_2 pollution around the world (2004–2014), J. Geophys. Res., 121, 976–996, doi:10.1002/2015JD024121, 2016.

Fischer, H., Birk, M., Blom, C., Carli, B., Carlotti, M., von Clarmann, T., Delbouille, L., Dudhia, A., Ehhalt, D., Endemann, M., Flaud, J. M., Gessner, R., Kleinert, A., Koopman, R., Langen, J., López-Puertas, M., Mosner, P., Nett, H., Oelhaf, H., Perron, G., Remedios, J., Ridolfi, M., Stiller, G., and Zander, R.: MIPAS: an instrument for atmospheric and climate research, Atmos. Chem. Phys., 8, 2151–2188, doi:10.5194/acp-8-2151-2008, 2008.

Funke, B., López-Puertas, M., von Clarmann, T., Stiller, G. P., Fischer, H., Glatthor, N., Grabowski, U., Höpfner, M., Kellmann, S., Kiefer, M., Linden, A., Mengistu Tsidu, G., Milz, M., Steck, T., and Wang, D. Y.: Retrieval of stratospheric NO_x from 5.3 and 6.2 µm nonlocal thermodynamic equilibrium emissions measured by Michelson Interferometer for Passive Atmospheric Sounding (MIPAS) on Envisat, J. Geophys. Res., 110, D09302, doi:10.1029/2004JD005225, 2005.

Gille, J., Barnett, J., Arter, P., Barker, M., Bernath, P., Boone, C., Cavanaugh, C., Chow, J., Coffey, M., Craft, J., Craig, C., Dials, M., Dean, V., Eden, T., Edwards, D. P., Francis, G., Halvorson, C., Harvey, L., Hepplewhite, C., Khosravi, R., Kinnison, D., Krinsky, C., Lambert, A., Lee, H., Lyjak, L., Loh, J., Mankin, W., Massie, S., McInerney, J., Moorhouse, J., Nardi, B., Packman, D., Randall, C., Reburn, J., Rudolf, W., Schwartz, M., Serafin, J., Stone, K., Torpy, B., Walker, K., Waterfall, A., Watkins, R., Whitney, J., Woodard, D., and Young, G.: High Resolution Dynamics Limb Sounder: Experiment overview, recovery, and validation of initial temperature data, J. Geophys. Res.-Atmos., 113, D16S43, doi:10.1029/2007JD008824, 2008.

Gille, J., Cavanaugh, C., Halvorson, C., Hartsough, C., Nardi, B., Rivas, M., Khosravi, R., Smith, L., and Francis, G.: Final correction algorithms for HIRDLS version 7 data, Proc. SPIE, 8511, 85110K, doi:10.1117/12.930175, 2012.

Haley, C. S. and Brohede, S.: Status of the Odin/OSIRIS stratospheric O_3 and NO_2 data products, Can. J. Phys., 85, 1177–1194, doi:10.1139/P07-114, 2007.

Hendrick, F., Van Roozendael, M., Kylling, A., Petritoli, A., Rozanov, A., Sanghavi, S., Schofield, R., von Friedeburg, C., Wagner, T., Wittrock, F., Fonteyn, D., and De Mazière, M.: Intercomparison exercise between different radiative transfer models used for the interpretation of ground-based zenith-sky and multi-axis DOAS observations, Atmos. Chem. Phys., 6, 93–108, doi:10.5194/acp-6-93-2006, 2006.

Hilboll, A., Richter, A., Rozanov, A., Hodnebrog, Ø., Heckel, A., Solberg, S., Stordal, F., and Burrows, J. P.: Improvements to the retrieval of tropospheric NO_2 from satellite – stratospheric correction using SCIAMACHY limb/nadir matching and comparison to Oslo CTM2 simulations, Atmos. Meas. Tech., 6, 565–584, doi:10.5194/amt-6-565-2013, 2013.

Ingmann, P., Veihelmann, B., Langen, J., Lamarre, D., Stark, H., and Courrèges-Lacoste, G. B.: Requirements for the GMES Atmosphere Service and ESA's implementation concept: Sentinels-4/-5 and -5p, Remote Sens. Environ., 120, 58–69, doi:10.1016/j.rse.2012.01.023, 2012.

Jonsson, A. I., de Grandpré, J., Fomichev, V. I., McConnell, J. C., and Beagley, S. R.: Doubled CO_2-induced cooling in the middle atmosphere: Photochemical analysis of the ozone radiative feedback, J. Geophys. Res., 109, D24103, doi:10.1029/2004JD005093, 2004.

Kalnay, E., Kanamisu, M., Kistler, R., Collins, W., Deaven, D., Gandin, L., Iredell, M., Saha, S., White, G., Woollen, J., Zhu, Y., Chelliah, M., Ebisuzaki, W., Higgins, W., Janowiak, J., Mo, K. C., Ropelewski, C., Wang, J., Leetmaa, A., Reynolds, R., Jenne, R., and Dennis, J.: The NCEP/NCAR 40 Year Reanalysis Project, B. Am. Meteorol. Soc., 77, 437–471, doi:10.1175/1520-0477(1996)077<0437:TNYRP>2.0.CO;2, 1996.

Kerzenmacher, T., Wolff, M. A., Strong, K., Dupuy, E., Walker, K. A., Amekudzi, L. K., Batchelor, R. L., Bernath, P. F., Berthet, G., Blumenstock, T., Boone, C. D., Bramstedt, K., Brogniez, C., Brohede, S., Burrows, J. P., Catoire, V., Dodion, J., Drummond, J. R., Dufour, D. G., Funke, B., Fussen, D., Goutail, F., Griffith, D. W. T., Haley, C. S., Hendrick, F., Höpfner, M., Huret, N., Jones, N., Kar, J., Kramer, I., Llewellyn, E. J., López-Puertas, M., Manney, G., McElroy, C. T., McLinden, C. A., Melo, S., Mikuteit, S., Murtagh, D., Nichitiu, F., Notholt, J., Nowlan, C., Piccolo, C., Pommereau, J.-P., Randall, C., Raspollini, P., Ridolfi, M., Richter, A., Schneider, M., Schrems, O., Silicani, M., Stiller, G. P., Taylor, J., Tétard, C., Toohey, M., Vanhellemont, F., Warneke, T., Zawodny, J. M., and Zou, J.: Validation of NO_2 and NO from the Atmospheric Chemistry Experiment (ACE), Atmos. Chem. Phys., 8, 5801–5841, doi:10.5194/acp-8-5801-2008, 2008.

Kim, J.: GEMS (Geostationary Environment Monitoring Spectrometer) onboard the GeoKOMPSAT to Monitor Air Quality in high Temporal and Spatial Resolution over Asia-Pacific Region, EGU General Assembly 2012, Vienna, Austria, 22–27 April 2012, 4051, 2012.

Krotkov, N. A., McLinden, C. A., Li, C., Lamsal, L. N., Celarier, E. A., Marchenko, S. V., Swartz, W. H., Bucsela, E. J., Joiner, J., Duncan, B. N., Boersma, K. F., Veefkind, J. P., Levelt, P. F., Fioletov, V. E., Dickerson, R. R., He, H., Lu, Z., and Streets, D. G.: Aura OMI observations of regional SO_2 and NO_2 pollution changes from 2005 to 2015, Atmos. Chem. Phys., 16, 4605–4629, doi:10.5194/acp-16-4605-2016, 2016.

Lamsal, L. N., Krotkov, N. A., Celarier, E. A., Swartz, W. H., Pickering, K. E., Bucsela, E. J., Gleason, J. F., Martin, R. V., Philip, S., Irie, H., Cede, A., Herman, J., Weinheimer, A., Szykman, J. J., and Knepp, T. N.: Evaluation of OMI operational standard NO_2 column retrievals using in situ and surface-based NO_2 observations, Atmos. Chem. Phys., 14, 11587–11609, doi:10.5194/acp-14-11587-2014, 2014.

Levelt, P. F., Van den Oord, G. H. J., Dobber, M. R., Mälkki, A., Visser, H., de Vries, J., Stammes, P., Lundell, J. O. V., and Saari, H.: The ozone monitoring instrument, IEEE T. Geosci. Remote Sens., 44, 1093–1101, doi:10.1109/TGRS.2006.872333, 2006.

Llewellyn, E. J., Lloyd, N. D., Degenstein, D. A., Gattinger, R. L., Petelina, S. V., Bourassa, A. E., Wiensz, J. . T., Ivanov, E. V., McDade, I. C., Solheim, B. H., McConnell, J. C., Haley, C. S., von Savigny, C., Sioris, C. E., McLinden, C. A., Griffioen, E., Kaminski, J., Evans, W. F. J., Puckrin, E., Strong, K., Wehrle, V., Hum, R. H., Kendall, D. J. W., Matsushita, J., Murtagh, D. P., Brohede, S., Stegman, J., Witt, G., Barnes, G., Payne, W. F., Piché, L., Smith, K., Warshaw, G., Deslauniers, D.-L., Marchand, P., Richardson, E. H., King, R. A., Wevers, I., McCreath, W., Kyrölä, E., Oikarinen, L., Leppelmeier, G. W., Auvinen, H., Mégie, G., Hauchecorne, A., Lefèvre, F., de La Nöe, J., Ricaud, P., Frisk, U., Sjoberg, F., von Schéele, F., and Nordh, L.: The OSIRIS instrument on the Odin spacecraft, Can. J. Phys., 82, 411–422, doi:10.1139/p04-005, 2004.

Marchenko, S., Krotkov, N. A., Lamsal, L. N., Celarier, E. A., Swartz, W. H., and Bucsela, E. J.: Revising the slant column density retrieval of nitrogen dioxide observed by the Ozone Monitoring Instrument, J. Geophys. Res.-Atmos., 120, 5670–5692 , doi:10.1002/2014JD022913, 2015.

Martin, R. V., Chance, K., Jacob, D. J., Kurosu, T. P., Spurr, R. J. D., Bucsela, E., Gleason, J. F., Palmer, P. I., Bey, I., Fiore, A. M., Li, Q., Yantosca, R. M., and Koelemeijer, R. B. A.: An im-

proved retrieval of tropospheric nitrogen dioxide from GOME, J. Geophys. Res.-Atmos., 107, 4437, doi:10.1029/2001JD001027, 2002.

McLinden, C. A., Olsen, S. C., Hannegan, B., Wild, O., Prather, M. J., and Sundet, J.: Stratospheric ozone in 3-D models: A simple chemistry and the cross-tropopause flux, J. Geophys. Res., 105, 14653–14665, doi:10.1029/2000JD900124, 2000.

McLinden, C. A., Haley, C. S., and Sioris, C. E.: Diurnal effects in limb scatter observations, J. Geophys. Res.-Atmos., 111, D14302, doi:10.1029/2005JD006628, 2006.

McLinden, C. A., Fioletov, V., Boersma, K. F., Krotkov, N., Sioris, C. E., Veefkind, J. P., and Yang, K.: Air quality over the Canadian oil sands: A first assessment using satellite observations, Geophys. Res. Lett., 39, L04804, doi:10.1029/2011GL050273, 2012a.

McLinden, C. A., Bourassa, A. E., Brohede, S., Cooper, M., Degenstein, D. A., Evans, W. J. F., Gattinger, R. L., Haley, C. S., Llewellyn, E. J., Lloyd, N. D., Loewen, P., Martin, R. V., McConnell, J. C., McDade, I. C., Murtagh, D., Rieger, L., Von Savigny, C., Sheese, P. E., Sioris, C. E., Solheim, B., and Strong, K.: Osiris: A Decade of scattered light, B. Am. Meteorol. Soc., 93, 1845–1863, doi:10.1175/BAMS-D-11-00135.1, 2012b.

Murtagh, D., Frisk, U., Merino, F., Ridal, M., Jonsson, A., Stegman, J., Witt, G., Eriksson, P., Jiménez, C., Megie, G., Noë, J. D. La, Ricaud, P., Baron, P., Pardo, J. R., Hauchcorne, A., Llewellyn, E. J., Degenstein, D. A., Gattinger, R. L., Lloyd, N. D., Evans, W. F. J., McDade, I. C., Haley, C. S., Sioris, C., von Savigny, C., Solheim, B. H., McConnell, J. C., Strong, K., Richardson, E. H., Leppelmeier, G. W., Kyrölä, E., Auvinen, H., and Oikarinen, L.: An overview of the Odin atmospheric mission, Can. J. Phys., 80, 309–319, doi:10.1139/p01-157, 2002.

Prather, M.: Catastrophic loss of stratospheric ozone in dense volcanic clouds, J. Geophys. Res., 97, 10187–10191, doi:10.1029/92JD00845, 1992.

Richter, A. and Burrows, J. P.: Tropospheric NO_2 from GOME measurements, Adv. Space Res., 29, 1673–1683, doi:10.1016/S0273-1177(02)00100-X, 2002.

Richter, A., Burrows, J. P., Nüß, H., Granier, C., and Niemeier, U.: Increase in tropospheric nitrogen dioxide over China observed from space, Nature, 437, 129–132, doi:10.1038/nature04092, 2005.

Rieger, L. A., Bourassa, A. E., and Degenstein, D. A.: Merging the OSIRIS and SAGE II stratospheric aerosol records, J. Geophys. Res., 12, 1–15, doi:10.1002/2015JD023133, 2015.

Russell, A. R., Valin, L. C., and Cohen, R. C.: Trends in OMI NO_2 observations over the United States: effects of emission control technology and the economic recession, Atmos. Chem. Phys., 12, 12197–12209, doi:10.5194/acp-12-12197-2012, 2012.

Schoeberl, M. R., Douglass, A. R., Hilsenrath, E., Bhartia, P. K., Beer, R., Waters, J. W., Gunson, M. R., Froidevaux, L., Gille, J. C., Barnett, J. J., Levelt, P. F., and DeCola, P.: Overview of the EOS aura mission, IEEE T. Geosci. Remote Sens., 44, 1066–1072, doi:10.1109/TGRS.2005.861950, 2006.

Scinocca, J. F., McFarlane, N. A., Lazare, M., Li, J., and Plummer, D.: Technical Note: The CCCma third generation AGCM and its extension into the middle atmosphere, Atmos. Chem. Phys., 8, 7055–7074, doi:10.5194/acp-8-7055-2008, 2008.

Sierk, B., Richter, A., Rozanov, A., Von Savigny, C., Schmoltner, A. M., Buchwitz, M., Bovensmann, H., and Burrows, J. P.: Retrieval and monitoring of atmospheric trace gas concentrations in nadir and limb geometry using the space-borne SCIAMACHY instrument, Environ. Monit. Assess., 120, 65–77, doi:10.1007/s10661-005-9049-9, 2006.

Sioris, C. E., Kurosu, T. P., Martin, R. V., and Chance, K.: Stratospheric and tropospheric NO_2 observed by SCIAMACHY: First results, Adv. Space Res., 34, 780–785, doi:10.1016/j.asr.2003.08.066, 2004.

Søvde, O. A., Gauss, M., Smyshlyaev, S. P., and Isaksen, I. S. A.: Evaluation of the chemical transport model Oslo CTM2 with focus on arctic winter ozone depletion, J. Geophys. Res., 113, D09304, doi:10.1029/2007JD009240, 2008.

van Geffen, J. H. G. M., Boersma, K. F., Van Roozendael, M., Hendrick, F., Mahieu, E., De Smedt, I., Sneep, M., and Veefkind, J. P.: Improved spectral fitting of nitrogen dioxide from OMI in the 405–465 nm window, Atmos. Meas. Tech., 8, 1685–1699, doi:10.5194/amt-8-1685-2015, 2015.

Veefkind, J. P., Boersma, K. F., Wang, J., Kurosu, T. P., Krotkov, N., Chance, K., and Levelt, P. F.: Global satellite analysis of the relation between aerosols and short-lived trace gases, Atmos. Chem. Phys., 11, 1255–1267, doi:10.5194/acp-11-1255-2011, 2011.

Zhou, Y., Brunner, D., Hueglin, C., Henne, S. and Staehelin, J.: Changes in OMI tropospheric NO_2 columns over Europe from 2004 to 2009 and the influence of meteorological variability, Atmos. Environ., 46, 482–495, doi:10.1016/j.atmosenv.2011.09.024, 2012.

Zoogman, P., Liu, X., Suleiman, R. M., Pennington, W. F., Flittner, D. E., Al-Saadi, J. A., Hilton, B. B., Nicks, D. K., Newchurch, M. J., Carr, J. L., Janz, S. J., Andraschko, M. R., Arola, A., Baker, B. D., Canova, B. P., Chan Miller, C., Cohen, R. C., Davis, J. E., Dussault, M. E., Edwards, D. P., Fishman, J., Ghulam, A., González Abada, G., Grutter, M., Herman, J. R., Houck, J., Jacob, D. J., Joiner, J., Kerridge, B. J., Kim, J., Krotkov, N. A., Lamsal, L., Li, C., Lindfors, A., Martin, R. V. and McElroy, C. T.: Tropospheric emissions: Monitoring of pollution (TEMPO), J. Quant. Spectrosc. Ra., doi:10.1016/j.jqsrt.2016.05.008, online first, 2016.